Development/Plasticity/Repair

β-Adrenergic Signaling Promotes Morphological Maturation of Astrocytes in Female Mice

Marci F. Rosenberg,[1,2] Marlesa I. Godoy,[3] Sarah D. Wade,[1,4] Mercedes F. Paredes,[5,6] Ye Zhang,[3] and Anna V. Molofsky[1,4,7]

[1]Department of Psychiatry and Behavioral Sciences and Weill Institute of Neurosciences, University of California at San Francisco, San Francisco, California 94143, [2]Medical Scientist Training Program and Biomedical Sciences Graduate Program, University of California at San Francisco, San Francisco, California 94143, [3]Department of Psychiatry and Biobehavioral Sciences, Semel Institute for Neuroscience and Human Behavior, David Geffen School of Medicine, University of California, Los Angeles, California 90095, [4]Neurosciences Graduate Program, University of California at San Francisco, San Francisco, California 94143, [5]Department of Neurology, Weill Institute of Neurosciences, University of California, San Francisco, San Francisco, California 94143, [6]Chan Zuckerberg Biohub-San Francisco, San Francisco, California 94158, and [7]Kavli Institute for Fundamental Neuroscience, University of California, San Francisco, San Francisco, California 94143

Astrocytes play essential roles in the developing nervous system, including supporting synapse function. These astrocyte support functions emerge coincident with brain maturation and may be tailored in a region-specific manner. For example, gray matter astrocytes have elaborate synapse-associated processes and are morphologically and molecularly distinct from white matter astrocytes. This raises the question of whether there are unique environmental cues that promote gray matter astrocyte identity and synaptogenic function. We previously identified adrenergic receptors as preferentially enriched in developing gray versus white matter astrocytes, suggesting that noradrenergic signaling could be a cue that promotes the functional maturation of gray matter astrocytes. We first characterized noradrenergic projections during postnatal brain development in mouse and human, finding that process density was higher in the gray matter and increased concurrently with astrocyte maturation. RNA sequencing revealed that astrocytes in both species expressed α- and β-adrenergic receptors. We found that stimulation of β-adrenergic receptors increased primary branching of rodent astrocytes *in vitro*. Conversely, astrocyte-conditional knockout of the β1-adrenergic receptor reduced the size of gray matter astrocytes and led to dysregulated sensorimotor integration in female mice. These studies suggest that adrenergic signaling to developing astrocytes impacts their morphology and has implications for adult behavior, particularly in female animals. More broadly, they demonstrate a mechanism through which environmental cues impact astrocyte development. Given the key roles of norepinephrine in brain states, such as arousal, stress, and learning, these findings could prompt further inquiry into how developmental stressors impact astrocyte development and adult brain function.

Key words: **β-adrenergic receptor; astrocyte; brain development; norepinephrine**

Significance Statement

This study demonstrates a role for noradrenergic signaling in the development of gray matter astrocytes. We provide new evidence that the β_1-adrenergic receptor is robustly expressed by both mouse and human astrocytes, and that conditional KO of the β_1-adrenergic receptor from female mouse astrocytes impairs gray matter astrocyte maturation. Moreover, female conditional KO mice exhibit behavioral deficits in two paradigms that test sensorimotor function. Given the emerging interest in moving beyond RNA sequencing to probe specific pathways that underlie astrocyte heterogeneity, this study provides a foundation for future investigation into the effect of noradrenergic signaling on astrocyte functions in conditions where noradrenergic signaling is altered, such as stress, arousal, and learning.

Received Feb. 20, 2023; revised June 24, 2023; accepted July 31, 2023.

Author contributions: M.F.R., M.I.G., M.F.P., Y.Z., and A.V.M. designed research; M.F.R. and M.I.G. performed research; M.F.R. and S.D.W. analyzed data; M.F.R. and A.V.M. wrote the paper; M.F.R., M.I.G., M.F.P., and A.V.M. edited the paper; M.F.P. contributed unpublished reagents/analytic tools.

This work was supported by National Institutes of Health R01MH119349 to A.V.M.; F30MH124367 to M.F.R.; R01NS109025 to Y.Z.; T32MH073526 to M.I.G.; and P01NS083513 and DP2NS122550-01 to M.F.P.; the Roberta and Oscar Gregory Endowment in Stroke and Brain Research to M.F.P.; and the Achievement Rewards for College Scientists Foundation Los Angeles Founder Chapter to M.I.G. We thank members of the A.V.M. laboratory for helpful comments on the manuscript; Gladstone Behavioral Core for assistance in behavioral testing and analysis; University of California at San Francisco Laboratory for Cell Analysis and Center for Advanced Technology for technical assistance; and Jae Yeon Kim and Alex Rezai for useful suggestions in optimization of human brain tissue staining. Schematics in Figures 2, 4-7 were created with BioRender.com.

The authors declare no competing financial interests.

Correspondence should be addressed to Anna V. Molofsky at anna.molofsky@ucsf.edu.

https://doi.org/10.1523/JNEUROSCI.0357-23.2023

Introduction

Astrocytes are morphologically complex cells that play essential roles in both the developing and adult brain, including promotion of synapse formation and elimination (Christopherson et al., 2005; Allen et al., 2012; Chung et al., 2013; Vainchtein et al., 2018), neurotransmitter recycling (Anderson and Swanson, 2000), and potassium buffering (Bellot-Saez et al., 2017). These functions are thought to be particularly relevant in the gray matter, where astrocyte processes are intimately associated with synapses. For example, a single hippocampal astrocyte has been estimated to contact >100,000 synapses (Bushong et al., 2002). In mouse models, gray matter astrocytes mature and increase in morphologic complexity between 0 and 30 postnatal days, partly driven by molecules, such as glutamate (Morel et al., 2014) and neuroligins (Stogsdill et al., 2017). Given the close link between astrocyte morphology and synaptic functions (Khakh and Sofroniew, 2015; Poskanzer and Molofsky, 2018), defining the signals that promote astrocyte morphologic complexity is critical to understanding the roles of astrocytes in brain development.

Many of these distinctive roles of gray matter astrocytes in synaptic support are thought to be driven by the physical association of astrocyte processes with synapses. For example, extension of astrocyte processes into the synaptic cleft enhances astrocytic glutamate uptake (Pannasch et al., 2014), while retraction of astrocyte processes from the synaptic cleft increases glutamate spillover (Badia-Soteras et al., 2023). In contrast, white matter astrocytes, by virtue of their anatomic location, engage with far fewer synapses than gray matter astrocytes (Finnema et al., 2016); they also have a distinctly less "bushy" morphology, with primary processes highly expressing the cytoskeletal protein GFAP, and few higher-order (secondary, tertiary, etc.) branches (Lundgaard et al., 2014). Our group previously compared the molecular profiles of developing gray versus white matter astrocytes in thalamus and spinal cord using a fluorescent reporter for the cytokine interleukin 33 (IL-33), which is highly enriched in gray matter astrocytes in early postnatal life (Vainchtein et al., 2018). Bulk RNA sequencing identified a number of signaling pathways that are enriched in IL-33$^+$ gray matter astrocytes. Of the neurotransmitter signaling pathways, adrenergic receptors were the most broadly upregulated, with 4 of 9 subtypes (*Adra1a, Adra2a, Adra2c, Adrb1*) enriched in gray matter astrocytes (Vainchtein et al., 2018).

Norepinephrine (NE) is a key neuromodulator and the primary ligand of adrenergic receptors in the brain. NE impacts many brain states, including arousal, sleep, learning, and response to stress (Sara, 2009; O'Donnell et al., 2012). A number of studies have demonstrated that adult astrocytes respond acutely to NE in the context of arousal, primarily via α-adrenergic receptors (Ding et al., 2013; Paukert et al., 2014). However, the role of noradrenergic signaling in astrocyte development or morphology is less clear. Here, we investigated the role of NE in postnatal astrocyte development. We found that the density of noradrenergic projections increased during postnatal brain maturation in the mouse, correlating with known trajectories of astrocyte morphologic maturation in rodents. While NE process density peaked earlier in human brains, consistent with known temporal differences in human versus rodent brain maturation, we found that noradrenergic innervation was strongly enriched in the gray matter relative to white matter in both mouse and human. RNA sequencing of astrocytes in both species detected abundant expression of β-adrenergic receptors, and *in situ* mouse studies revealed dynamic regional and temporal differences in expression. Pharmacological stimulation of β-adrenergic receptors increased rodent astrocyte complexity *in vitro*, while conditional KO (cKO) of the β_1-adrenergic receptor from astrocytes at birth decreased the size of gray, but not white, matter astrocytes in female mice. Moreover, postnatal conditional deletion of the β_1-adrenergic receptor in astrocytes led to impaired balance beam performance and enhanced prepulse inhibition (PPI) in female mice, suggestive of altered sensorimotor integration. These results reveal a developmental pathway by which astrocytic β_1-adrenergic signaling promotes gray matter astrocyte morphologic maturation and impacts adult brain function.

Materials and Methods

Mice. All mouse strains were maintained in a specific pathogen-free facility at University of California at San Francisco (UCSF), and all animal protocols were approved by and in accordance with the guidelines established by the Institutional Animal Care and Use Committee and Laboratory Animal Resource Center. Littermate controls were used for all experiments when feasible. For the NE transporter (NET) developmental time course and *Adrb1* ISH time course, heterozygous *Aldh1l1*^{eGFP} (MGI:3843271) mice were used. For RNA sequencing of regionally specified astrocytes, WT mice on a C57BL6/J background (maintained in-house for >3 generations) were used. For the N-(2-chloroethyl)-N-ethyl-2-bromobenzylamine (DSP-4) experiments, Swiss Webster mice (Taconic; postnatal astrocyte labeling by electroporation [PALE]), or C57BL6/J mice (NET validation) were used, and were injected with vehicle (normal saline) or 50 mg/kg DSP-4 (2958, Tocris Bioscience) dissolved in normal saline at P14 and P21 (PALE labeling), or at P5 (NET validation).

The astrocyte-conditional *Adrb1* KO was made using the following breeding strategy: *Adrb1*$^{fl/fl}$ (Mani et al., 2016) mice were crossed with *Adrb1*$^{fl/fl}$; *Aldh1l1*$^{CreERT2+}$ (RRID:IMSR_JAX:031008) hemizygous animals. At P1, all pups were given an intragastric injection of tamoxifen (T5648; Sigma-Aldrich). To make the tamoxifen, a stock solution (at 10 mg/ml) was made in corn oil (C8267; Sigma-Aldrich). After dissolving overnight, a working solution (final concentration 2.5-4 mg/ml) was made fresh the day of injection by further diluting in corn oil, and used at a concentration of 100 mg/kg. Control animals had a genotype of *Adrb1*$^{fl/fl}$, while Adrb1 conditional KO (cKO) animals had a genotype of *Adrb1*$^{fl/fl}$; *Aldh1l1*$^{CreERT2+}$.

Immunohistochemistry: mouse. Mice were transcardially perfused with 1 ml/g (capping at ~10 ml) of ice-cold 1× PBS, followed by 1 ml/g (capping at ~10 ml) of 4% PFA (P6148; Sigma-Aldrich). Brains were then postfixed at 4°C for a minimum of 4 h in 4% PFA, and then transferred to 30% sucrose (S0389; Sigma-Aldrich) until they were fully submerged. After embedding and freezing in OCT compound (25608-930; VWR), brains were sectioned at 50 µm thickness on a CryoStar NX70 Cryostat (Fisher Scientific), and collected into 24-well plates containing 1× PBS with 0.05% sodium azide. Sections were blocked and permeabilized at room temperature for 1 h in a 1× PBS solution containing 5% normal goat serum (S26, Millipore Sigma) and 0.4% Triton X-100 (T9284, Sigma-Aldrich). Following blocking, primary antibody diluted in the same blocking solution was added to the tissues, and they were stained overnight at 4°C. Primary antibodies were used at the following concentrations: mouse anti-NET (1:1000, MAb Technologies, NET05-2); chick anti-GFP (1:1000, Aves Labs GFP-1020); rat anti-GFAP (1:1000, Invitrogen 13-0300); and rabbit anti-mCherry (1:1000, Fisher Scientific M11217). Sections were then washed 3× for 5 min in a 1× PBS solution containing 0.05% Triton X-100 (PBST), incubated in secondary antibody diluted 1:500 in blocking solution for 1.5-2 h at room temperature, stained with Hoechst (1:10,000, Fisher Scientific 62249) for 5 min to label nuclei, washed 3× for 5 min in PBST, and mounted on coverslips with Fluoromount G (Southern Biotechnology 0100-01). The following goat secondary antibodies were used corresponding to the appropriate primary antibodies: AlexaFluor-488, AlexaFluor-555, and AlexaFluor-647 (Fisher Scientific). For the NET staining, before blocking, 10 min of antigen retrieval in a 0.01 M sodium citrate solution, pH 6, at 75°C was performed.

Human tissue sample collection. Collection was at postmortem intervals <24 h. Tissue was collected with previous patient consent to institutional ethical regulations of the UCSF Committee on Human Research. Protocols were approved by the Human Gamete, Embryo and Stem Cell Research Committee (Institutional Review Board GESCR #10-02693) at UCSF. Specimens collected from UCSF were evaluated by a neuropathologist as control samples collected via the UCSF Pediatric Neuropathology Research Laboratory. Tissues were cut coronally and areas of interest were sampled. Blocks used for histologic analyses were fixed with 4% PFA for 2 d, and cryoprotected in a 30% sucrose gradient. The tissue was then frozen in OCT and blocks were cut at 30 μm with a cryostat and mounted onto glass slides. For each case, cresyl staining of three sections spanning the block was used to ensure the appropriate position using anatomic landmarks, such as the lateral ventricle, and presence of the caudate, thalamus, and hippocampus.

Immunohistochemistry: human. Before starting staining, slides were allowed to come to room temperature, and then baked at 57°C for 30 min. Slides were washed in 1× PBS for 5 min 2×, and then 1× TBS for 5 min 1×. We then performed 10 min of antigen retrieval in a 0.01 M sodium citrate solution, pH 6, at 95°C. Slides were allowed to cool in their staining container for 20 min before proceeding. Slides were then washed in 1× TBS for 5 min 3×, and then blocked and permeabilized for 1 h at room temperature in a 1× TBS solution containing 5% BSA (A0336, Sigma-Aldrich) and 0.5% Triton X-100. Next, primary antibody diluted in the same blocking solution was added to the slides, and they were stained overnight at 4°C. Primary antibodies were used at the following concentrations: rabbit anti-dopamine-β-hydroxylase (DBH) (1:250, Sigma-Aldrich SAB2701977), mouse anti-Aldh1l1 (1:250, Antibodies N103/39), and chick anti-NeuN (1:500, EMD Millipore ABN91). Following 3 × 5 min wash in 1× TBS, secondary antibody diluted 1:300 in 5% BSA in 1× TBS was added to the slides, and they were incubated for 2 h at room temperature. Following another 3 × 5 min wash in 1× TBS, slides were mounted on coverslips with DAPI Fluoromount-G (0100-20, Southern Biotechnology). The following goat secondary antibodies were used corresponding to the appropriate primary antibodies: AlexaFluor-488, AlexaFluor-555, and AlexaFluor-647 (Fisher Scientific).

NET and DBH quantification. Slides were imaged on an LSM800 confocal microscope (Zeiss). For the NET staining, a 20× objective was used to collect 1 or 2 stacks of 12.8 μm per region per mouse. For the DBH staining, a 10× objective with the widefield configuration was used to collect 2 or 3 stacks of 10.35 μm per region per slide. Using ImageJ, maximum intensity projections of each stack were made, and then loaded into SNT (version 4.1.5) (Arshadi et al., 2021), an ImageJ plug-in optimized for tracing of neuronal morphology. For NET tracings, before loading the projections into SNT, a thresholded (binarized) image of the NET channel was first made by manually thresholding to the ~95th percentile of the histogram. The image was then masked to eliminate spurious, punctate background noise, excluding all signal < 1 μm^2. Using this thresholded and masked NET image, the "Autotrace Segmented Image" function within SNT was then deployed, using the following settings (Discard small components < 1 μm; Connect adjacent components < 6 μm apart) to create automatic reconstructions. Each reconstruction was manually checked against the original image to ensure accuracy, and edited as necessary. For DBH tracings, the traditional SNT semi-automated tracing functionality was used. For both, after completing tracings, the total length of NET^+/DBH^+ segments in the image was measured, and then divided by the μm^3 volume of the image to output final NET^+/DBH^+ density.

FACS of astrocytes. Astrocytes were isolated and purified for sorting based on a previously published protocol (Molofsky et al., 2014). Briefly, mice were transcardially perfused with ~10 ml of ice-cold 1× PBS, and cortical versus subcortical tissue was microdissected using a dissecting microscope. After mincing the tissue with a razor blade, the tissue was enzymatically dissociated into a single-cell suspension with an HBSS-Ca/Mg free solution containing 20 units/ml papain (LS003126, Worthington Biochemical) and supplemented with L-cysteine, EDTA, glucose, and DNase. Tissue was dissociated in a 34°C water bath for 60 min; every 10 min, the tissue was gently mechanically agitated. After using a trypsin inhibitor (LS003086, Worthington Biochemical) solution (in HBSS-Ca/Mg free buffer, supplemented with glucose, BSA, and DNase) to stop dissociation, cells were spun down at 300 × *g* for 5 min at room temperature, and the pellet was resuspended with up to 10 triturations with a P1000 pipette tip, until all large chunks were broken up and the solution looked homogeneous. To deplete myelin, cells were run through a 22% Percoll gradient at 900 × *g*, no brake at 4°C for 20 min, after which cells were incubated with 1 μl CD16/CD32 (14-0161-82, eBioscience), 0.6 μl CD11b-PE (12-0112-81, eBioscience), and 0.75 μl ACSA-2-APC (130-117-535, Miltenyi Biotec) in a 100 μl HBSS-Ca/Mg free solution supplemented with HEPES, glucose, and EDTA. After staining for 20 min, cells were spun down at 300 × *g* for 5 min at 4°C, and then resuspended in the same solution they were stained in, minus the antibodies. A purified astrocyte population, defined as ACSA-$2^{high}CD11b^{neg}$ was collected by FACS on a BD Aria3 (BD Biosciences) into 1.5 ml Eppendorf tubes. After sorting, cells were spun down at 500 × *g* for 10 min at 4°C, and then lysed in 350 μl RLT Plus (74034, QIAGEN), and vortexed for 5 s. Lysed cells were stored at −80°C. For qPCR and bulk RNA sequencing, astrocyte RNA was processed as described below.

qPCR. After thawing the lysed astrocytes in RLT Plus buffer, mRNA was isolated from each sample using the RNeasy Plus Micro Kit (74034, QIAGEN). mRNA was converted to cDNA using the High Capacity cDNA Reverse Transcription Kit (4374966, Invitrogen). Primers for *Adrb1* (Mm00431701_s1) and *Aldh1l1* (Mm00550947_m1) were purchased from TaqMan (Fisher Scientific), and qPCR was performed using a Fast SYBR Green Master Mix (43-856-12, Fisher Scientific) with a 7900HT Fast Real-Time PCR System (Applied Biosystems). Data were then analyzed with SDS software version 2.4 (Applied Biosystems).

Bulk RNA sequencing of astrocytes. A total of 30,000 to 50,000 astrocytes were sorted per region per sample (mouse) from a total of 4 mice. RNA was isolated as above, in the qPCR section. After RNA isolation, RNA concentration and quality were assessed with the Agilent RNA 6000 Pico kit on Bioanalyzer. All samples had an RNA integrity score > 8. cDNA libraries were then prepared using a QuantSeq 3′ mRNA-Seq Library Prep Kit FWD for Illumina (Lexogen). Per-sample cDNA concentrations were confirmed via qPCR, and samples were then pooled and single-end sequenced for 65 cycles (SE65) on an Illumina HiSeq 4000, yielding a read depth of 5-8 million reads/sample.

Samples were analyzed as previously described (Vainchtein et al., 2018; R. T. Han et al., 2023). Briefly, after assessing read quality with FastQC (version 0.11.5; https://www.bioinformatics.babraham.ac.uk/projects/fastqc/), samples were aligned to the *Mus musculus* genome (Ensembl GRC m39) using STAR aligner (version 2.6.0) (Dobin et al., 2013). Aligned reads were then counted with HTSeq (version 0.9.0) (Anders et al., 2015), and loaded into R, where count normalization and differential expression analysis (between cortical vs subcortical astrocytes) was performed using DESeq2 (version 1.35.0) (Love et al., 2014). Bulk RNA-seq data of astrocytes from P29 cortical versus subcortical tissue (see Fig. 3*A*,*B*) is available from GEO with accession number GSE235840.

ISH. For ISH analysis of *Adrb1* in astrocytes, 14 μm sections of brain tissue were prepared on Fisherbrand Superfrost Plus Microscope slides (12-550-15, Fisher Scientific) using a CryoStar NX70 Cryostat (Fisher Scientific). Using probes targeted against *Adrb1* and *Aldh1l1*, the RNAscope Multiplex Fluorescent V2 assay kit (ACD) was used, followed by, when appropriate, our typical mouse immunostaining protocol (see above) using chick anti-GFP (1:1000, Aves Labs GFP-1020) to amplify astrocytic GFP signal from $Aldh1l1^{eGFP}$ mice. To analyze these slides, 5 μm stacks using a 40× objective on a Zeiss LSM800 confocal microscope were taken. After making maximum intensity projections of these stacks in ImageJ, *Adrb1* puncta within astrocytic soma (as marked by GFP labeling when on an $Aldh1l1^{eGFP}$ background, or colabeling with *Aldh1l1* puncta) were manually counted. For the astrocytic *Adrb1* time course (see Fig. 3), at least three FOVs per region per mouse were quantified. For the validation of astrocytic *Adrb1* knockdown in our *Adrb1* cKO model (see Fig. 5), at least 2 FOVs per region per mouse (10 nonastrocytic cells/region for specificity quantifications; at least 10 cerebellar astrocytes/mouse for in situ validation of knockdown) were quantified.

Immunopanning. Rat astrocytes were purified according to a previously published immunopanning protocol using both male and female rats (Foo, 2013). Briefly, six 150-mm-diameter Petri dishes were coated with 25 ml of 50 mM Tris-HCl (pH 9.5) and 60 μl of species-specific

secondary antibodies, and one plate was coated 60 μl of BSL-1 (L-100, Vector Labs) in place of secondary antibody. The next day, all plates except the BSL-1 plate were washed 3 times with 1× PBS and coated with primary antibodies (20 μl antibody in 12 ml buffer [0.2% BSA in DPBS] per panning plate): rat anti-mouse CD45 (BD550539, BD Biosciences), mouse anti-human integrin β-5 (ITGB5) (14-0497-82, eBioscience), or a hybridoma supernatant against O4 (4 ml hybridoma supernatant in 8 ml buffer per panning plate), respectively. Cerebral cortices from P6-P7 neonatal rats of mixed sex were dissected in PBS and meninges removed. Tissue was dissociated with 12 units/ml papain (NC9597281, Fisher Scientific) at 34.5°C for 45 min. Tissue was then mechanically triturated with a 5 ml serologic pipette in the presence of trypsin inhibitor solution. Endothelial cells, microglia/macrophages, and oligodendrocyte precursor cells were depleted from the single-cell suspension by incubating the suspension sequentially on the secondary antibody only, BSL-1, CD45, and O4 antibody-coated Petri dishes. Finally, the single-cell suspension was incubated on the ITGB5 antibody-coated Petri dish. After washing away nonadherent cells with PBS, astrocytes bound to the ITGB5 antibody-coated Petri dish were lifted using trypsin, and then plated on poly-D-lysine-coated plastic coverslips at a density of 20,000 cells per well in 24-well plates in a serum-free medium containing DMEM (11960069, Invitrogen), Neurobasal (21103049, Invitrogen), sodium pyruvate (11360070, Invitrogen), glutamine (25030081, Invitrogen), *N*-acetyl cysteine (A8199, Sigma), and heparin-binding EGF-like growth factor (E4643, Sigma). Half the volume of media was replaced every 48 h with fresh media until cells were collected.

For the drug treatments, stock solutions at a concentration of 1 mM diluted in 1× PBS were made for each of the following pharmacological compounds: NE (A7256-1G, Sigma), isoproterenol (1747, Tocris), phenylephrine (P6126-5G, Sigma), and dexmedetomidine (SML0956-10MG, Sigma). All compounds were added to the astrocytes on the fifth day after plating (5 DIV) at a final concentration of 1 μM. One to 3 wells per treatment condition were used per batch (three batches total). Cells were incubated at 37°C for 3 h after treatment was added. After drug treatment, a live membrane stain, CellMask Green Plasma Stain (C37608, Fisher Scientific), was added to each well at a 1:1000 dilution. Cells were incubated at 37°C for 13 min, then washed with 1× PBS one time and fixed with 4% PFA (50-980-495, Fisher Scientific) for 15 min at room temperature. Cells were then washed twice with 1× PBS and mounted on glass slides (12-550-15, Fisher Scientific) using Prolong Antifade media with DAPI (P36935, Fisher Scientific) and stored at −20°C until imaged. Coverslips were imaged at 20× on a Carl Zeiss Apotome epifluorescent microscope. Four or 5 images per coverslip (well) were taken. Primary processes were manually counted in ImageJ. For the process length measurements, all separately distinguishable cells in at least 2 FOVs per condition (at least 8 cells per condition) were semiautomatically traced using SNT (version 4.1.5).

PALE. Astrocytes were labeled based on a previously published protocol for PALE (Stogsdill et al., 2017). Briefly, a membrane-tagged astrocyte reporter plasmid, pZac2.1-gfaABC1D-mCherry-CAAX (a kind gift from Cagla Eroglu), was injected into the lateral ventricles of P1 mice using a Kopf stereotaxic apparatus (David Kopf Instruments) with a microdispensing pump (World Precision Instruments) holding a beveled needle with a ∼50-μm-diameter tip, and then electroporated with five 100 V/50 ms pulses (950 ms interpulse interval) using an ECM 830 square wave electroporator system (BTX), with the positive electrode positioned roughly over the cortex. After intraperitoneal injections of DSP-4 at P14 and P21, animals were killed at P24 and tissue was processed, sectioned, and stained as above, with the exception that tissue was sectioned thicker, at 100 μm, to better capture entire astrocytes. All permeabilization and staining times were thus extended, with initial blocking/permeabilization lasting for 4 h, staining in primary antibody solution 2× overnight at 4°C, and staining in secondary antibody solution 1× overnight at 4°C. All washes were also extended to 15 min.

Individual cortical astrocytes (region: cortical layers IV-VI) were imaged on an LSM780 confocal microscope (Zeiss) using a 63× objective. As much of the entire astrocyte as could be visualized was captured in a *z* stack. The internal complexity analysis was completed in ImageJ. For this analysis, a single optical section per cell that captured the largest cut of the cell without an apparent $DAPI^+$ nucleus in the cell soma was picked. A median filter with 2 pixel radius was then used to smooth the astrocyte membrane signal. After using the magic wand function to create a tight perimeter around the signal, the signal was then thresholded using the Otsu automated algorithm to obtain a final output of astrocyte membrane signal within the perimeter. The GFAP-per-cell analysis was completed in Imaris (version 9.8). For this analysis, after creating a surface of each astrocyte, the mean fluorescent intensity (MFI) of GFAP within the surface was measured. Because each astrocyte was collected at a different depth within the thick sections, and antibody penetration generally decreases as you move further interior into the section, the GFAP MFI was then normalized to the astrocytic mCherry-CAAX signal (e.g., for each cell, the GFAP MFI was divided by the mCherry MFI), and this normalized GFAP MFI was then plotted.

Viral astrocytic labeling. For single-astrocyte morphologic analysis in the Adrb1 cKO model, an astrocyte reporter virus, pAAV5-gfaABCD1D-LckGFP (105598, Addgene), was injected into the lateral ventricle of P1-P3 mice using the same stereotactic setup as above. After killing the mice at P25-P26, tissue was processed and sectioned at 50 μm, and stained as described above. Individual astrocytes (regions: layer V/VI of somatosensory cortex; corpus callosum) were imaged on a LSM800 confocal microscope (Zeiss), using a 40× objective coupled with 1.5-2.0 optical zoom. A15 μm stack was then collected per cell, centered around the middle approximately one-third of the astrocyte, encompassing the soma. All analyses were completed in Imaris (version 9.8). After creating a surface of each astrocyte, the maximum diameter (Ellipsoid Axis Length C × 2) and, for cortical astrocytes, GFAP MFI, were measured.

Behavior. All behavioral assays were run on a total of 59 mice (31 control, 28 Adrb1 cKO), separated over two cohorts. Each animal was run in the same order (elevated plus maze, open field, balance beam, PPI) across assays, with experimenter blind to genotype.

For the open field test, animals were habituated to the testing room for 1 h before being placed in the activity chamber (41 × 41 × 30 cm) for 15 min of recorded exploration per mouse. Activity was automatically detected and measured via breaks in photobeam arrays using the FlexField/Open Field Photobeam Activity System (San Diego Instruments). In between each mouse, the chamber was cleaned with 70% ethanol.

For the elevated plus maze, animals were habituated to a dimly lit testing room for 1 h before being placed in the elevated plus maze apparatus for 10 min of recorded exploration. The elevated plus maze is composed of two open arms (without walls) and two closed arms (with 6.5-inch-tall walls). As before, movement was automatically detected and measured via breaks in photobeam arrays, and information about time spent/distance traveled in the open versus closed arm was collected. In between each mouse, the chamber was cleaned with 70% ethanol.

For the PPI assay, individual animals were placed in a restraining chamber positioned within a larger sound attenuating box, to ensure each animal was only responding to the stimulus in the assay, and not any spurious noise or movement. The restraining chamber was equipped with floor electrode motion sensors that could detect and register the magnitude of any reflexive flinching response (startle) by the animal. After 5 min of habituation to the restraining chamber at a 64 dB background noise, acoustic stimulus testing started. For 20 min, mice were exposed to a series of 120 dB acoustic stimuli that either were or were not preceded by a weaker acoustic stimulus. Each mouse was subjected to a series of 80 trials, in random order, that consisted of 24 baseline startle response trials (120 dB for 40 ms), 14 low-dB PPI trials (4 dB prepulse for 40 ms followed by 120 dB for 40 ms), 14 medium-dB PPI trials (15 dP prepulse for 40 ms followed by 120 dB for 40 ms), 14 high-dB PPI trials (26 dB prepulse for 40 ms followed by 120 dB for 40 ms), and 12 no-stimulus trials (to measure baseline activity). Interstimulus interval varied between 8 and 22 s, with a mean of 15 s. In between each mouse, the restraining chamber was cleaned with 70% ethanol.

For the balance beam assay, animals were tested for 3 consecutive days, with a 1 h habituation period before the start of testing. The balance beam consists of an open platform on one side (where the mice start) and the dark enclosure on the other side (the goal box), 41 cm away from the start. On day 1, each mouse was guided through two trials

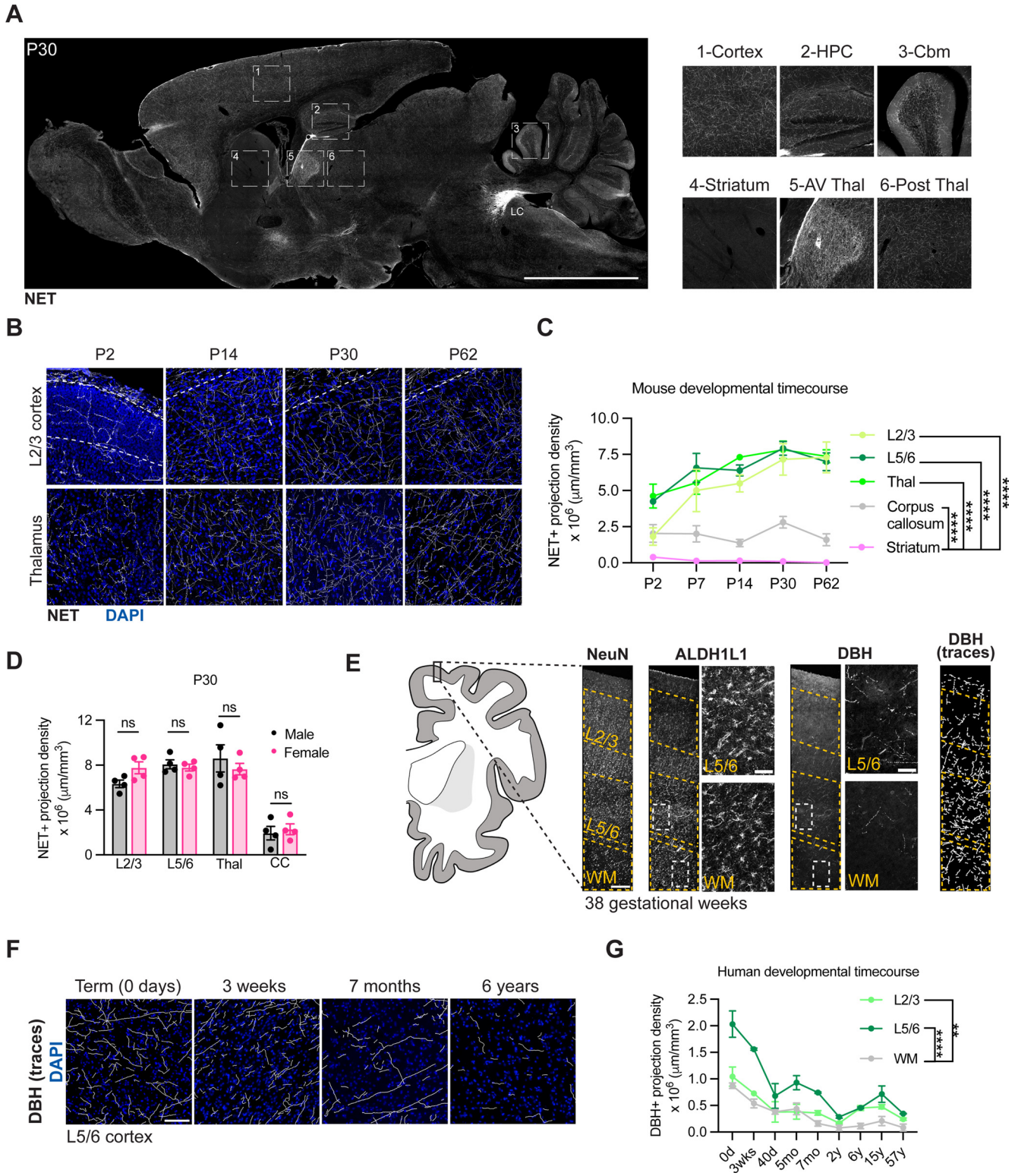

Figure 1. Developmental changes in noradrenergic innervation in mouse and human brain. ***A***, NET staining in postnatal day 30 (P30) sagittal brain section at level of locus coeruleus (LC). Scale bar, 100 μm. Insets, Differential NET density across mouse brain regions. HPC, Hippocampus; Cbm, cerebellum; AV Thal, anteroventral thalamus; Post thal, posterior thalamus. ***B***, Representative images of NE projection innervation in cortex and thalamus over postnatal development. Scale bar, 50 μm. ***C***, Quantification of NE projection innervation in cortex, thalamus, corpus callosum, and striatum. L2/3, layer II/III cortex; L5/6, layer V/VI cortex; Thal, thalamus. Statistics: two-way ANOVA with Dunnett's multiple comparisons test (two-way ANOVA, region × age interaction, $F_{(4,69)} = 123.7$, $p < 0.0001$; multiple comparisons, $^{****}p < 0.0001$ between corpus callosum and each other region). Data are mean ± SEM, 3 or 4 mice per time point. ***D***, Quantification of NE projection density across brain regions at P30, separated by sex. L2/3, layer II/III cortex; L5/6, layer V/VI cortex; Thal, thalamus; CC, corpus callosum. Statistics: two-way ANOVA with Sidak's multiple comparisons (two-way ANOVA, sex × region interaction, $F_{(1,24)} = 0.09198$, $p = 0.7643$; multiple comparisons, each between male versus female mice, L2/3, ns, $p = 0.3718$; L5/6, ns, $p = 0.9951$; Thal, ns, $p = 0.7246$; CC, ns, $p = 0.9909$). Data are mean ± SEM. Dots represent individual mice. ***E***, Schematic and representative images of human brain analyses (Extended Data Fig. 1-1). Representative images show DBH staining from cortex of gestational week 38 human brain tissue. Scale bars: wide FOV images of NeuN, ALDH1L1, DBH, DBH traces, 250 μm; insets for ALDH1L1 and DBH, 50 μm. L2/3, layer II/III cortex; L5/6, layer V/VI cortex; WM, white matter. ***F***, Tracings of NE projection innervation as labeled by DBH immunostaining in human brain cortex at indicated time points. Scale bar, 100 μm. ***G***, Quantification of NE projection density in cortex and white

on the large (1.9 cm width) balance beam as training. Ten to 15 minutes after training, each mouse had three unguided trials on the large balance beam. On the next day, each mouse had three unguided trials on the medium (1.1 cm width) balance beam. On the third and last day, each mouse had three unguided trials on the small (0.5 cm width) balance beam. Intertrial interval was 10-15 min. Latency to cross and number of falls were scored live, while balance checks and foot slips were manually scored by watching video recordings on reduced speed. Any slip of a limb below the beam was counted as a foot slip. In between each mouse, the beam was cleaned with 70% ethanol.

Data analysis. Experimental design details are included in the methods description and figure legends. For statistical analysis, GraphPad Prism 8 and 9, and R (for normalization of counts after RNA sequencing, as described above) were used. The statistical tests used in each analysis, accompanied by the corresponding statistical values, are specified in the appropriate figure legends.

Results

Developmental changes in noradrenergic innervation in mouse and human brain

To examine the maturation of the mouse noradrenergic system in gray and white matter, we quantified noradrenergic (NE) projection density using an antibody targeted against NET to label both NE neuronal somas (which primarily reside in the locus coeruleus in the pons) and their projections. We found that, by postnatal day 30 (P30), much of the mouse brain was uniformly innervated by NE projections (Fig. 1*A-C*), which was consistent between sexes (Fig. 1*D*). Of notable difference, the anteroventral thalamus was densely innervated, while the striatum was virtually devoid of NE projections (Fig. 1*A*).

We observed that NE projection density rapidly increased during early postnatal development across multiple gray matter brain regions, including the thalamus and cortex, largely reaching adult density of $\sim 6.5 \times 10^6$ μm processes/mm^3 by P14 (Fig. 1*B*,*C*). In contrast, white matter brain regions, including the corpus callosum, maintained a consistently low NE projection density ~4-fold lower than gray matter regions (Fig. 1*C*). Given the correlation between relative density of NE projections and tissue content of NE in the brain (Elias et al., 1982; Oke et al., 1983), these data suggest an increase in NE tone during postnatal brain maturation, consistent with other studies (Latsari et al., 2002), and further indicate that this increase is selective to gray matter brain regions. Of note, cortical astrocyte maturation largely occurs in the first postnatal month in mice (Morel et al., 2014; Stogsdill et al., 2017), overlapping with the time period during which we observed an increase in NE process density.

To evaluate whether this pattern of maturation is conserved in humans, we examined the development of the NE system in the human brain, across ages ranging from infancy to adulthood (Extended Data Fig. 1-1). We labeled noradrenergic neurons with an antibody targeted against DBH, the enzyme catalyzing the final step in the synthesis of NE. We then quantified NE projection density in two regions with particularly disparate densities in the mouse: cortex and white matter. As in mice, both superficial and deep cortical layers had higher projection density than the subcortical white matter (Fig. 1*E-G*). Overall NE projection density in human gray matter was substantially lower than in mice (~0.2-2 $\times$ 10^6 μm processes/mm^3 in humans vs ~2-7.5 $\times$ 10^6 μm processes/mm^3 in mice). Furthermore, in human tissue, NE process density was highest at term (39 gestational weeks) and decreased thereafter (Fig. 1*G*).

While direct developmental comparisons between mouse and human brain can be challenging and region-specific (Semple et al., 2013), it was notable that, in both mouse and human tissue, noradrenergic process density was preferentially enriched in the gray matter relative to white matter, raising the question of how NE promotes brain maturation in these two regions.

Early postnatal ablation of NE reduces astrocyte morphologic complexity

To probe whether NE impacts astrocyte maturation, we used the noradrenergic toxin DSP-4 to ablate NE projections (Jaim-Etcheverry and Zieher, 1980; Nowak, 2016) during development. We then examined astrocyte morphology and molecular identity. Astrocytes were sparsely labeled with a membrane-tagged astrocyte reporter plasmid (gfaABC1D-mCherry-CAAX) at P1, using PALE (Stogsdill et al., 2017). We intraperitoneally injected noradrenergic toxin DSP-4 at P14 and P21 and then killed the mice at P25 (Fig. 2*A*), when mouse cortical astrocytes reach their peak complexity (Morel et al., 2014; Stogsdill et al., 2017). A similar neonatal DSP-4 injection paradigm achieved robust ablation of forebrain NE projections (Fig. 2*B*). To assess morphologic maturation, we imaged individual cortical astrocytes, and analyzed a single optical section per astrocyte that captured the largest cross-section of the cell. The amount of membrane-bound mCherry signal contained within the astrocyte's perimeter was quantified as a readout of astrocyte branch complexity, a metric we term "membrane density." We found that cortical astrocytes from DSP-4-treated animals had reduced membrane density (Fig. 2*C*,*D*) as well as increased GFAP expression, particularly in their primary processes (Fig. 2*E*,*F*). While these data are limited by the caveats of toxin-mediated ablation and were not robustly powered, they suggested the possibility that NE signaling could impact astrocyte morphology, raising the question of which adrenergic receptors might mediate these effects.

Profiling of astrocytic adrenergic receptors in mouse and human

To determine whether forebrain astrocytes were competent to respond to NE signaling during development, we examined the region-specific expression of astrocytic adrenergic receptors via bulk RNA sequencing of FACS-isolated astrocytes collected from microdissected cortical and subcortical tissue (Fig. 3*A*). We used ACSA-2 staining to selectively purify astrocytes from P29 C57BL6/J mice (Batiuk et al., 2017, 2020) (Fig. 3*A*). We compared our results with a previously published P7 astrocytic transcriptomic dataset, which also isolated astrocytes from both the cortical and subcortical tissue (Herrero-Navarro et al., 2021). Across developmental ages, we found that 4 of the 9 subtypes of adrenergic receptors were expressed by astrocytes, with at least one of each receptor class expressed (Fig. 3*B*). At both P7 and P29, the most highly expressed adrenergic receptors, particularly in subcortical tissue, were *Adra2a* and *Adrb1* (Fig. 3*B*). In humans, we previously showed that astrocytes isolated from cortical surgical specimens also express adrenergic receptors (Krawczyk et al., 2022), with *ADRB1* and *ADRB2* expressed most highly (Fig. 3*C*). Admittedly, a snapshot of RNA expression provides a limited readout of adrenergic receptor protein activity, which is both temporally and spatially regulated (Fu and Xiang, 2015). Nevertheless,

←

matter of human brain. L2/3, layer II/III cortex; L5/6, layer V/VI cortex; WM, white matter. Statistics: two-way ANOVA with Dunnett's multiple comparisons (two-way ANOVA, region $\times$ age interaction, $F_{(2,27)} = 63.50$, $p < 0.0001$; multiple comparisons, ****$p < 0.0001$ between L5/6 and white matter, **$p = 0.0098$ between L2/3 and white matter). Data are mean ± SEM, 2 slides per age.

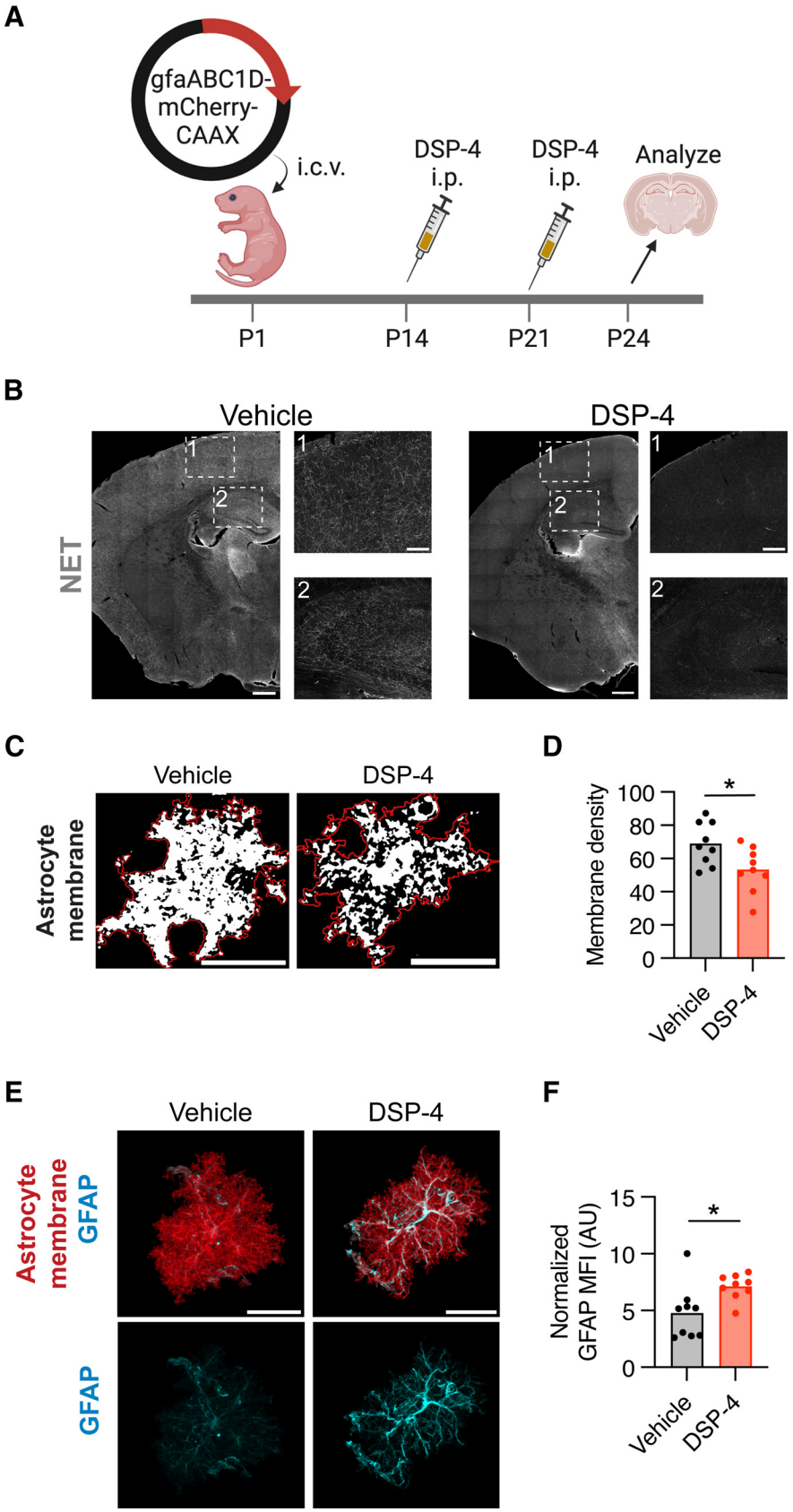

Figure 2. Early postnatal ablation of NE reduces astrocyte morphologic complexity. ***A***, Experimental timeline for astrocyte sparse labeling by plasmid electroporation at P1 followed by DSP-4-mediated NE ablation at P14-P21. ***B***, Representative images illustrating extent of NE projection ablation at P25 following intraperitoneal injection of DSP-4 at P5. Insets: (1) cortex; (2) hippocampus. Scale bars: coronal brain hemi-sections, 500 μm; insets, 150 μm. ***C***, Representative images of thresholded cortical astrocyte single optical sections from vehicle and DSP-4-treated conditions. Red line indicates the perimeter of the cell. White thresholded signal represents the astrocyte membrane enclosed within the perimeter. Scale bar, 25 μm. ***D***, Quantification of cortical astrocyte membrane density, defined as the percent of the astrocyte's cross-sectional area covered by plasma membrane. Statistics: two-tailed, unpaired *t* test ($t_{(16)} = 2.521$, $^*p = 0.0227$).

these data suggest that astrocytes in the human and mouse forebrain may be competent to respond to NE signaling.

Given the strong expression of the β_1-adrenergic receptor in both mouse and human astrocytes, and a dearth of data about this particular receptor in astrocytes (in contrast to α-adrenergic signaling), we further quantified *Adrb1* expression in developing mouse brain via quantitative FISH. Astrocytes across the brain expressed *Adrb1* by P7 (Fig. 3*D*,*E*); and in the thalamus and cerebellum, *Adrb1* was predominantly expressed by astrocytes at P7 (Fig. 3*D*). Over the first month of development, we generally observed consistent astrocytic *Adrb1* expression but found a reduction in expression in thalamic astrocytes, and an increase in cerebellar astrocytes (Fig. 3*E*). While cerebellar *Adrb1* expression stayed fairly restricted to astrocytes, in the thalamus, we also observed a robust increase in *Adrb1* expression in nonastrocytes, presumably neurons (Fig. 3*D*). We also assessed whether there were any sex-specific differences in astrocytic *Adrb1* expression. We found that, at both P7 and P30, astrocytic *Adrb1* expression significantly differed by sex, and at P30, there was a significant increase in *Adrb1* expression in female versus male pontine astrocytes (Fig. 3*F*). These data show that *Adrb1* is expressed by astrocytes across multiple brain regions in the first month of postnatal development, that this expression is temporally dynamic in the thalamus and cerebellum, and that expression patterns vary between sexes.

β and α_2 signaling have opposing effects on astrocyte branching *in vitro*

Adrenergic receptors are GPCRs with distinct cellular impacts (Philipp and Hein, 2004). The α_1 receptor signals through the inositol trisphosphate pathway, causing an increase in intracellular calcium. In contrast, the α_2 and β receptors signal through the adenosine cAMP pathway to either decrease (α_2) or increase (β) cAMP levels (Fig. 4*A*). To evaluate whether specific adrenergic pathways mediate unique effects on astrocyte maturation, we first turned to an *in vitro* system, purifying rat cortical astrocytes by immunopanning (Foo, 2013) and culturing them in serum-free media. Immunopanned astrocytes form processes in culture (Foo et al., 2011), thus allowing us to test compounds that affect astrocyte branching, which we used as a proxy for astrocyte maturation (Morel et al., 2014; Stogsdill et al., 2017).

To determine the impact of noradrenergic signaling on astrocyte branching, we treated immunopanned astrocytes at 5 days *in vitro* (DIV) with adrenergic receptor-specific agonists targeting these distinct subclasses. We added 1 μM of each of the following compounds: NE, the α_1 agonist phenylephrine, the α_2 agonist dexmedetomidine, or the nonselective β agonist isoproterenol. Doses were chosen based on pilot experiments and existing literature (Shain et al., 1987; Sherpa et al., 2016; Kitano et al., 2021). Three hours after treatment, cells were fixed, and plasma membrane was labeled with a CellMask stain to visualize cell processes (Fig. 4*B*). Importantly, previous studies have found that transcriptomes are highly similar between *in vivo* and immunopanned cultured astrocytes (Foo et al., 2011). When we specifically examined adrenergic receptor expression in P7 *in vivo* (acutely purified) astrocytes compared with *in vitro* (immunopanned) astrocytes, we indeed observed consistent expression levels (Fig. 4*C*). We used two metrics to quantify process branching: the number of primary processes per cell, measured from the cell soma, as well as the total process length of all processes in an individual cell. We observed significant impacts of all selective agonists on astrocyte branching within the 3 h treatment window (Fig. 4*D-F*). Both the α_1 and β agonists increased the number of primary processes and the total process length/cell. In contrast, the α_2 agonist decreased branching and process length (Fig. 4*E*,*F*). Interestingly, β and α_2 agonists have opposing effects on cAMP levels (Fig. 4*A*), which suggests that astrocyte process extension could be regulated by levels of cAMP, or its downstream products. Of note, NE alone had a nonsignificant trend toward increased process length, possibly as a result of opposing effects of different receptor subclasses. Together, these data show that adrenergic signaling can rapidly mediate changes in astrocyte morphology *in vitro*, and that α_1 and β agonists increase astrocyte branching, whereas α_2 agonists decrease branching.

Astrocyte-specific deletion of the β_1-adrenergic receptor in neonatal mice

To test the cell-autonomous role of β_1-adrenergic signaling on postnatal astrocyte development *in vivo*, we conditionally deleted the β_1 receptor from neonatal astrocytes. We crossed the astrocyte-specific Cre line *Aldh1l1*^{CreERT2} (Srinivasan et al., 2016) with an *Adrb1* floxed allele (Mani et al., 2016), and administered a single intragastric injection of tamoxifen at P1 (100 μg/g). To validate the efficiency of *Cre*-mediated excision, we isolated astrocytes from the whole brain (excluding cerebellum and brainstem) by FACS at P30 and performed qPCR for *Adrb1* (Fig. 5*A*). We observed a reproducible and consistent reduction in *Adrb1* expression in ACSA-2$^+$ astrocytes by ~85% (relative decrease of 84.9 ± 4.6% compared with astrocyte marker gene *Aldh1l1* expression) (Fig. 5*B*). To evaluate specificity of our conditional deletion strategy, we used quantitative ISH to evaluate *Adrb1* expression in nonastrocytes of adult animals. We found no changes in nonastrocytic *Adrb1* expression in multiple brain regions, including the cortex and thalamus (Fig. 5*C*,*D*). In these same tissues, we confirmed robust knockdown of *Adrb1* expression in *Aldh1l1*$^+$ astrocytes (Fig. 5*E*,*F*), focusing on the cerebellum, where astrocytes are the predominant cells expressing *Adrb1* (Fig. 3*D*). Therefore, this model enables us to examine the direct effects of noradrenergic signaling through the β_1 receptor on astrocytes.

Noradrenergic signaling through the astrocytic β_1-adrenergic receptor increases gray matter astrocyte size in female mice

We next evaluated the impact of postnatal β_1-adrenergic signaling on gray and white matter astrocyte morphology, using the conditional deletion model established above (Fig. 5). We sparsely labeled astrocytes via intracerebroventricular injection of a viral astrocyte reporter construct expressing membrane-bound GFP (pAAV5-gfaABCD1D-LckGFP; Fig. 6*A*,*B*), and examined astrocyte morphology at P25-P26, focusing on maximum diameter to better capture the whole-cell effect of this perturbation. Of note, we observed that *Adrb1* expression was substantially higher in gray matter cortical astrocytes compared with white matter astrocytes in the corpus callosum (Fig. 6*C*), which prompted us to

←

Data points are individual cells, 9 cells (3 mice) per condition. ***E***, Representative images of per-cell GFAP intensity after DSP-4 treatment. Images represent the masked mCherry-CAAX (red) and GFAP (cyan) signal from an Imaris surface reconstruction of a single cortical astrocyte. Scale bar, 25 μm. ***F***, Quantification of normalized GFAP intensity (normalized to mCherry signal). AU, Arbitrary units. Statistics: Mann–Whitney test ($U_{(16)} = 13$, $^*p = 0.0142$). Data points are individual cells, 9 cells (3 mice) per condition.

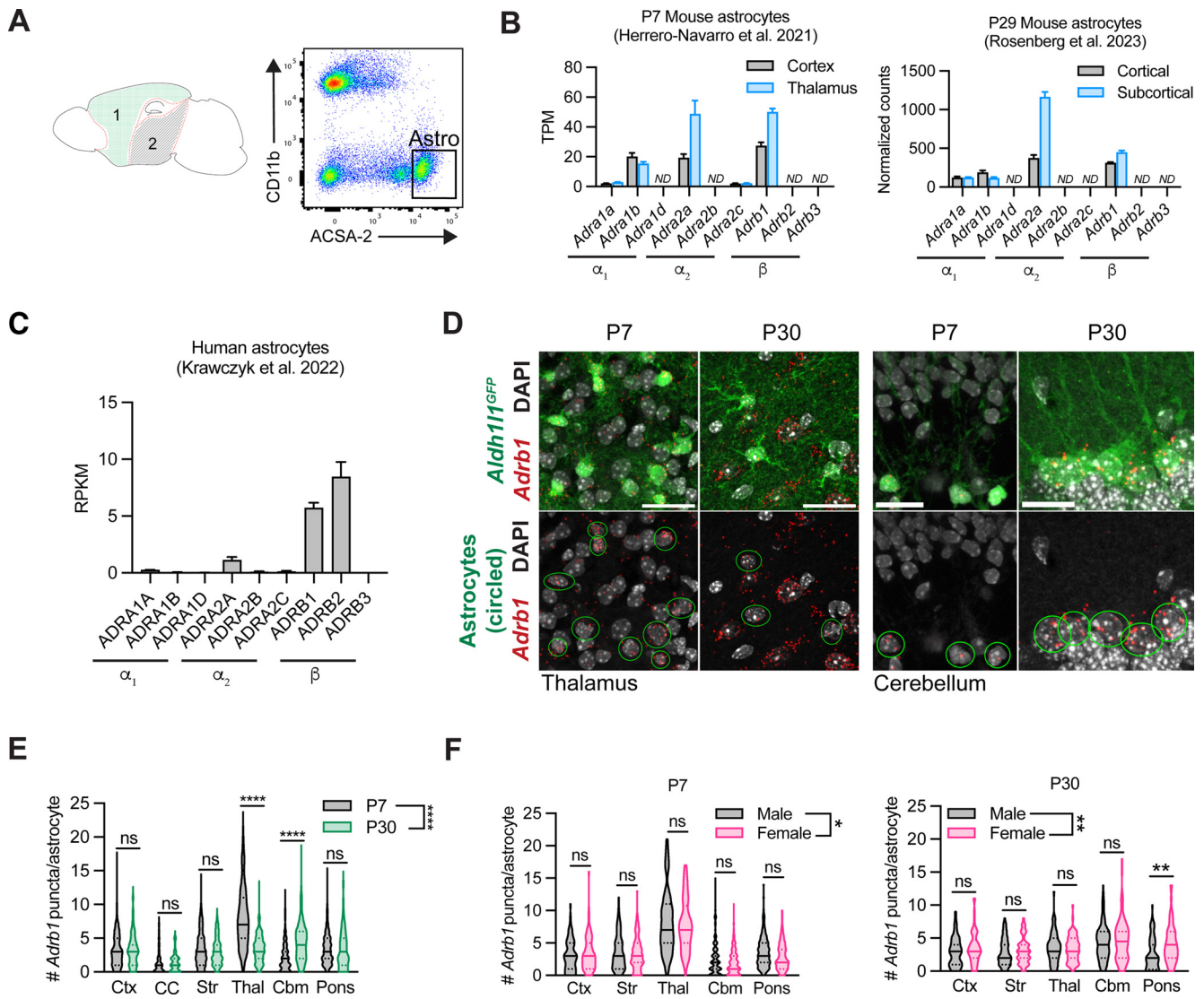

Figure 3. Profiling of astrocytic adrenergic receptors in mouse and human. ***A***, Schematic of regions dissected from P29 mouse brain for astrocyte RNA sequencing and representative flow plots of ACSA-2^{+} astrocytes isolated from cortical tissue. 1, cortical; 2, subcortical. ***B***, Adrenergic receptor expression in P7 (Herrero-Navarro et al., 2021) and P29 murine astrocytes isolated from cortical versus subcortical tissue of mouse. ND, Not detected. For the P7 dataset, gene expression is represented by transcripts per million (TPM) counts. Data are mean ± SEM, 4 mice per region. For the P29 dataset, counts normalized to per-sample library size. Data are mean ± SEM, 4 mice per region. ***C***, Adrenergic receptor expression in human cortical astrocytes. RPKM, reads per kilobase of transcript per million mapped reads. Data are mean ± SEM, 12 samples. ***D***, Representative images of *Adrb1* expression in astrocytes at P7 versus P30 in thalamus and cerebellum. Scale bars: thalamus, 25 μm; cerebellum, 15 μm. ***E***, Quantification of per-astrocyte *Adrb1* expression at P7 versus P30, across multiple brain regions. Ctx, Cortex; CC, corpus callosum; Str, striatum; Thal, thalamus; Cbm, cerebellum. Statistics: two-way ANOVA with Sidak's multiple comparisons (two-way ANOVA, region × age, $F_{(1,\ 2431)} = 12.054$, $p = 0.0005$; multiple comparisons, each between P7 versus P30, Ctx, ns, $p > 0.9999$; CC, ns, $p > 0.9999$; Str, ns, $p = 0.5836$; Thal, ****$p < 0.0001$; Cbm, ****$p < 0.0001$, Pons, ns, $p = 0.9996$). Data are median ± interquartile range (violin plots), plotted by cell, 4-6 mice per time point (P7 Ctx, $n = 163$ cells; P30 Ctx, $n = 111$ cells; P7 CC, $n = 91$ cells; P30 CC, $n = 62$ cells; P7 Str, $n = 324$ cells; P30 Str, $n = 137$ cells; P7 Thal, $n = 251$ cells; P30 Thal, $n = 143$ cells; P7 Cbm, $n = 482$ cells; P30 Cbm, $n = 263$ cells; P7 Pons, $n = 271$ cells; P30 Pons, $n = 145$ cells). ***F***, Quantification of per-astrocyte *Adrb1* expression in males versus females at P7 and P30, across multiple brain regions. Ctx, cortex; Str, striatum; Thal, thalamus; Cb, cerebellum. P7 statistics: two-way ANOVA with Sidak's multiple comparisons (two-way ANOVA, region × sex, $F_{(1,1542)} = 3.989$, *$p = 0.0460$; multiple comparisons, each between M versus F, Ctx, ns, $p = 0.9935$; Str, ns, $p = 0.9380$; Thal, ns, $p = 0.7225$; Cbm, ns, $p = 0.4922$; Pons, ns, $p = 0.1999$). Data are median ± interquartile range (violin plots), plotted by cell, 3 mice per sex (M P7 Ctx, $n = 74$ cells; F P7 Ctx, $n = 89$ cells; M P7 Str, $n = 162$ cells; F P7 Str, $n = 162$ cells; M P7 Thal, $n = 134$ cells; F P7 Thal, $n = 116$ cells; M P7 Cbm, $n = 288$ cells; F P7 Cbm, $n = 256$ cells; M P7 Pons, $n = 169$ cells; F P7 Pons, $n = 102$ cells). P30 statistics: two-way ANOVA with Sidak's multiple comparisons (two-way ANOVA, region × sex, $F_{(1790)} = 7.958$, **$p = 0.0049$; multiple comparisons, each between M versus F, Ctx, ns, $p = 0.6832$; Str, ns, $p = 0.9943$; Thal, ns, $p > 0.9999$; Cbm, ns, $p = 0.7845$; Pons, **$p = 0.0012$). Data are median ± interquartile range (violin plots), plotted by cell, 3 mice per sex (M P30 Ctx, $n = 55$ cells; F P30 Ctx, $n = 56$ cells; M P30 Str, $n = 80$ cells; F P30 Str, $n = 57$ cells; M P30 Thal, $n = 69$ cells; F P30 Thal, $n = 74$ cells; M P30 Cbm, $n = 128$ cells; F P30 Cbm, $n = 136$ cells; M P30 Pons, $n = 80$ cells; F P30 Pons, $n = 65$ cells).

examine both gray and white matter astrocytes in subsequent experiments. We found that, in female mice, cortical astrocytes in β_1 cKO animals had a significant reduction in their maximum diameter relative to littermate controls (Fig. 6*D*,*E*), and a significant increase in GFAP expression (Fig. 6*F*,*G*). Astrocytes from male cKO mice, however, showed no significant difference in maximum diameter or GFAP expression compared with littermate controls (Fig. 6*D-G*). Moreover, we observed no difference in maximum diameter of white matter astrocytes of the corpus callosum between genotypes in either sex (Fig. 6*H*,*I*), consistent with lower white matter expression of β_1 receptors. These data suggest that NE signaling via astrocytic β_1 receptors preferentially impacts gray matter astrocyte morphology in female mice.

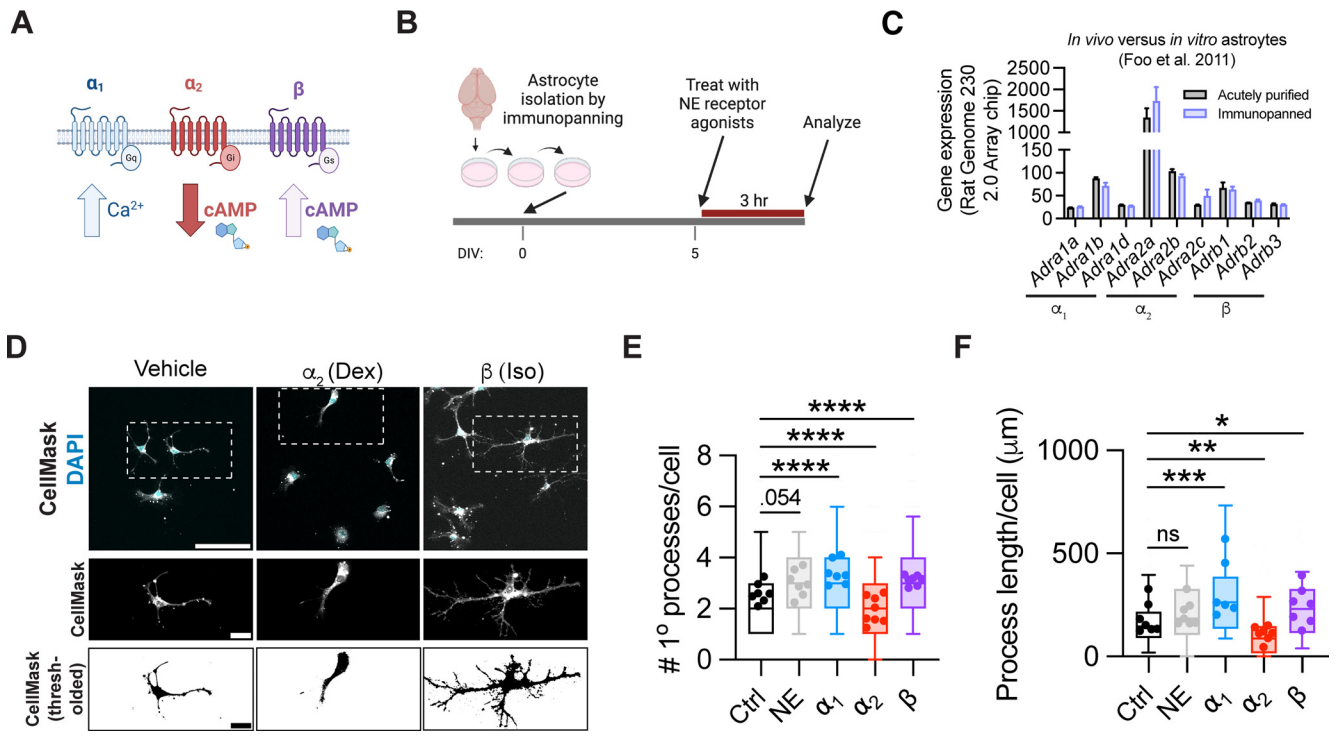

Figure 4. β and α_2 signaling have opposing effects on astrocyte branching *in vitro*. ***A***, Schematic of three different subclasses of adrenergic GPCRs. ***B***, Schematic of experimental design, based on rat cortical astrocytes purified by serial immunopanning. ***C***, Adrenergic receptor gene expression in acutely purified versus immunopanned rat astrocytes, as reported off of an Affymetrix Rat Genome 230 2.0 Array chip (Foo et al., 2011). ***D***, Representative images of immunopanned astrocytes treated with adrenergic receptor subtype-specific agonists. First row, raw image; second row, inset of individual cells; third row, thresholding of individual cells. Scale bars: first row, 100 μm; second row, 25 μm; third row, 25 μm. Dex, Dexmedetomidine; Iso, isoproterenol. ***E***, Quantification of astrocyte primary process count per cell 3 h after addition of the indicated agonists. List of agonists (all administered at 1 μM): NE; α_1, phenylephrine; α_2, dexmedetomidine, β, isoproterenol. Statistics: Kruskal–Wallis test with Dunn's multiple comparisons test, run on per-cell data ($H_{(1600)} = 157.8$, $p < 0.0001$; multiple comparisons, each between drug treatment and control, NE, ns, $p = 0.0537$; α_1, ****$p < 0.0001$; α_2, ****$p < 0.0001$, β, ****$p < 0.0001$). Data are median ± interquartile range (box and whiskers plot) with whiskers extending from 10th-90th percentile, plotted by cell, from 7 or 8 wells across 3 batches (Ctrl, $n = 298$ cells; NE, $n = 298$ cells; $\alpha_1 = 288$ cells; $\alpha_2 = 368$ cells; $\beta = 353$ cells). Per-well averages are superimposed on top of each box and whisker plot. ***F***, Quantification of total length of all astrocyte processes per cell, 3 h after addition of indicated agonists (same as in ***E***). Statistics: Kruskal–Wallis test with Dunn's multiple comparisons test, run on per-cell data ($H_{(482)} = 70.14$, $p < 0.0001$; multiple comparisons, each between drug treatment and control, NE, ns, $p = 0.2004$; α_1, ***$p = 0.0002$; α_2, **$p = 0.0012$, β, *$p = 0.0207$). Data are median ± interquartile range (box and whiskers plot) with whiskers extending from 10th-90th percentile, plotted by cell, from 6 or 7 wells across 3 batches (Ctrl, $n = 107$ cells; NE, $n = 95$ cells; $\alpha_1 = 68$ cells; $\alpha_2 = 109$ cells; $\beta = 108$ cells). Per-well averages are superimposed on top of each box and whisker plot.

Early postnatal astrocyte-conditional loss of β_1-adrenergic receptor impairs motor coordination and increases PPI in female mice

To determine whether the reduced gray matter astrocyte size induced by developmental loss of astrocytic *Adrb1* expression impacted brain function, we performed a series of behavioral assays to test somatosensation and sensorimotor function in two cohorts of animals with astrocyte-specific β_1 deletion versus littermate controls (Fig. 7*A*). Given the developmental dynamics of astrocytic *Adrb1* expression in the cerebellum and thalamus (Fig. 3*E*), we specifically wanted to evaluate behaviors for which those regions serve as important neural substrates. To assess cerebellar function, we used the balance beam assay, where mice crossed a 41-cm-long/1.9-cm-wide beam in each of three trials (Fig. 7*B*). We found that female, but not male, cKO mice exhibited an increased latency to cross the beam, coupled with an increased number of foot slip errors (Fig. 7*C*,*D*).

To evaluate sensorimotor gating, a process for which the thalamus is of particular importance, we used a PPI assay, which measures an animal's ability to appropriately dampen its startle response when prechallenged with a lower-magnitude acoustic stimulus (Fig. 7*E*). Similarly, we found that female, but not male, cKO mice showed enhanced startle inhibition (Fig. 7*F*,*G*), suggestive of an overreactive sensorimotor gating response. Other parameters were largely intact, with no changes in overall mobility in an open field apparatus (Fig. 7*H*) or anxiety-related behaviors, as assessed by performance in an elevated plus maze, (Fig. 7*I*). Together, these behavioral deficits suggest a sex-specific impact of β_1-adrenergic receptor signaling on astrocytic functional maturation and integration into behaviorally relevant circuits.

Discussion

In this study, we investigated the effect of noradrenergic signaling on astrocyte development, identifying a specific role for astrocytic β_1-adrenergic signaling in promoting the morphologic and functional maturation of developing gray matter astrocytes. We first characterized the development of the NE system in mouse and human, finding that NE process density rapidly increases in gray matter during brain development (Fig. 1). Given the effects on mouse cortical astrocyte morphology we observed after developmental ablation of NE projections with DSP-4 (Fig. 2), we were interested to see whether we could narrow this effect to a particular arm of the adrenergic signaling pathway. Profiling of adrenergic receptor expression in mouse and human astrocytes via bulk RNA sequencing revealed expression of all classes (α_1, α_2, and β) of receptors in both species, although human astrocytes predominantly expressed β receptors (Fig. 3). When adrenergic receptor-

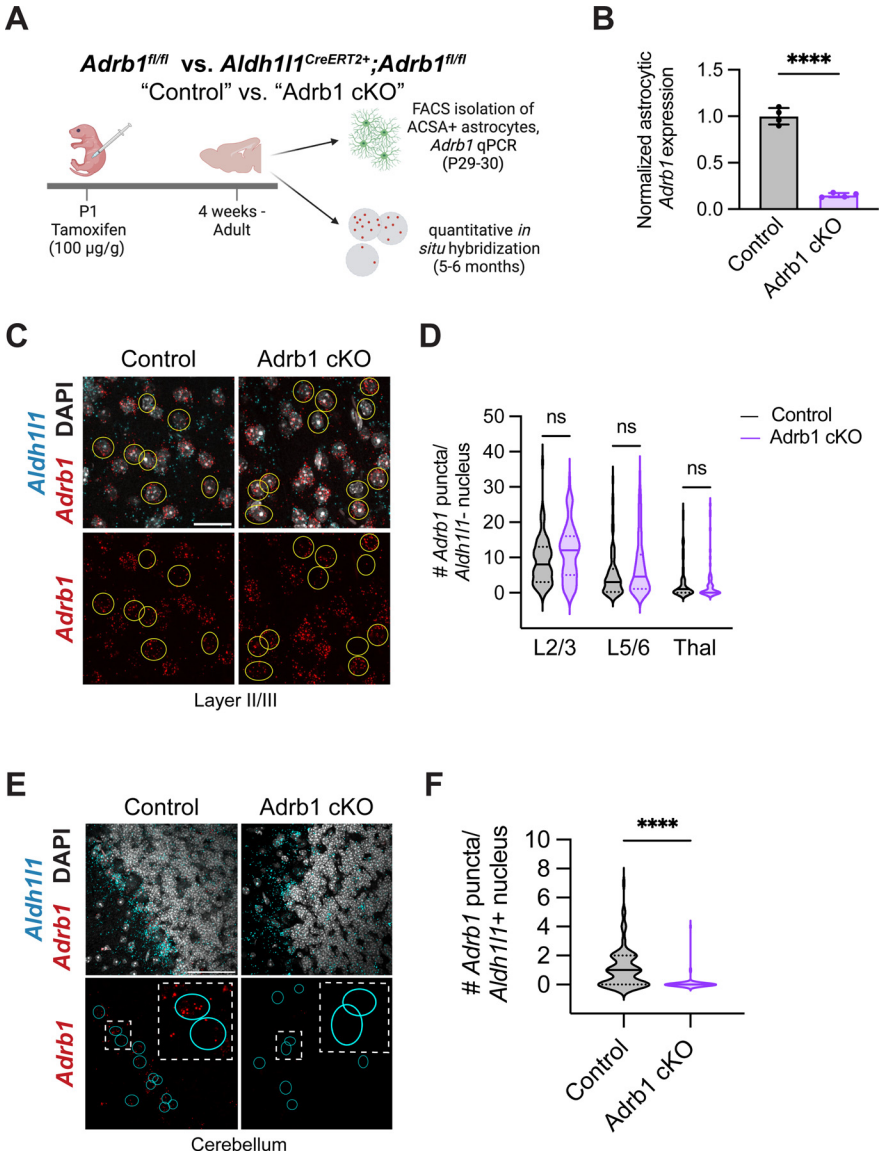

Figure 5. Astrocyte-specific deletion of the β_1-adrenergic receptor in neonatal mice. ***A***, Schematic for conditional deletion of *Adrb1* in astrocytes and validation of sensitivity and specificity. ***B***, Astrocytic *Adrb1* expression in astrocytes isolated from control (*Adrb1*$^{fl/fl}$) versus Adrb1 cKO (*Aldh1l1*$^{CreERT2+}$*Adrb1*$^{fl/fl}$) brains, as measured by qPCR, and normalized to astrocyte marker gene *Aldh1l1*. Dots represent individual animals. Statistics: two-tailed unpaired *t* test ($t_{(6)} = 18.40$, $^{****}p < 0.0001$). Data are mean ± SD. ***C***, Representative images of *Adrb1* fluorescent *ISH* in cortex of control versus Adrb1 cKO brains. Yellow circles outline nonastrocytic soma, around which perinuclear puncta were quantified. Scale bar, 25 µm. ***D***, Quantification of *Adrb1* puncta in non-astrocytes of control versus Adrb1 cKO animals in cortex and thalamus. L2/3, layer II/III cortex; L5/6, layer V/VI cortex; Thal, thalamus. Statistics: Welch's ANOVA with Dunnett's T3 multiple comparisons ($W_{(5,\ 209.3)} = 18.82$, $p < 0.0001$; multiple comparisons, each between genotypes per region, L2/3, ns, $p = 0.1286$; L5/6, ns, $p = 0.2264$, Thal, ns, $p = 0.9722$). Data are median ± interquartile range (violin plots), plotted by cell, 3 or 4 mice per genotype (L2/3 Control, $n = 81$ cells; L2/3 Adrb1 cKO, $n = 80$ cells; L5/6 Control, $n = 80$ cells; L5/6 Adrb1 cKO, $n = 80$ cells; Thal Control, $n = 80$ cells; Thal Adrb1 cKO, $n = 60$ cells). ***E***, Representative images of *Adrb1* expression in cerebellar astrocytes of control versus Adrb1 cKO animals. Cyan circles outline *Aldh1l1*$^+$ astrocytes. Scale bar, 50 µm. ***F***, Quantification of per-cell *Adrb1* puncta in cerebellar astrocytes of control versus Adrb1 cKO animals. Statistics: Mann–Whitney test ($U_{(147)} = 1257$, $^{****}p < 0.0001$). Data are median ± interquartile range (violin plots), plotted by cell, 4 mice per genotype (Control, $n = 82$ cells; Adrb1 cKO, $n = 67$ cells).

specific agonists were applied to astrocytes *in vitro*, we observed that stimulation of all adrenergic receptors affected astrocyte process branching, with activation of the α_1 and β receptors increasing astrocyte branching, while activation of the α_2 receptors decreased branching (Fig. 4). Given the enriched expression of β receptors in both mouse and human astrocytes, coupled with the astrocytic pro-branching effect we observed with β receptor stimulation *in vitro*, we developed a model for astrocyte-conditional deletion of the β_1 receptor in neonatal mice to probe this pathway *in vivo* (Fig. 5). We found that early postnatal astrocyte-conditional KO of the β_1 receptor reduced gray matter, but not white matter, astrocyte size (Fig. 6) in female mice, and that adult female cKO animals exhibited impaired sensorimotor function (Fig. 7).

Astrocytes are molecularly heterogeneous (Molofsky et al., 2014; Lanjakornsiripan et al., 2018; Bayraktar et al., 2020), and astrocyte heterogeneity is both developmentally patterned and shaped by environmental cues (Molofsky et al., 2012; Bayraktar et al., 2014). Evidence for environmental cues driving gray versus white matter astrocyte heterogeneity includes lineage tracing experiments showing that a single progenitor can give rise to both gray and white matter astrocytes in the mouse cortex (Clavreul et al., 2019). Moreover, human glial progenitor cells transplanted into the forebrain of postnatal day 1 (P1) mice

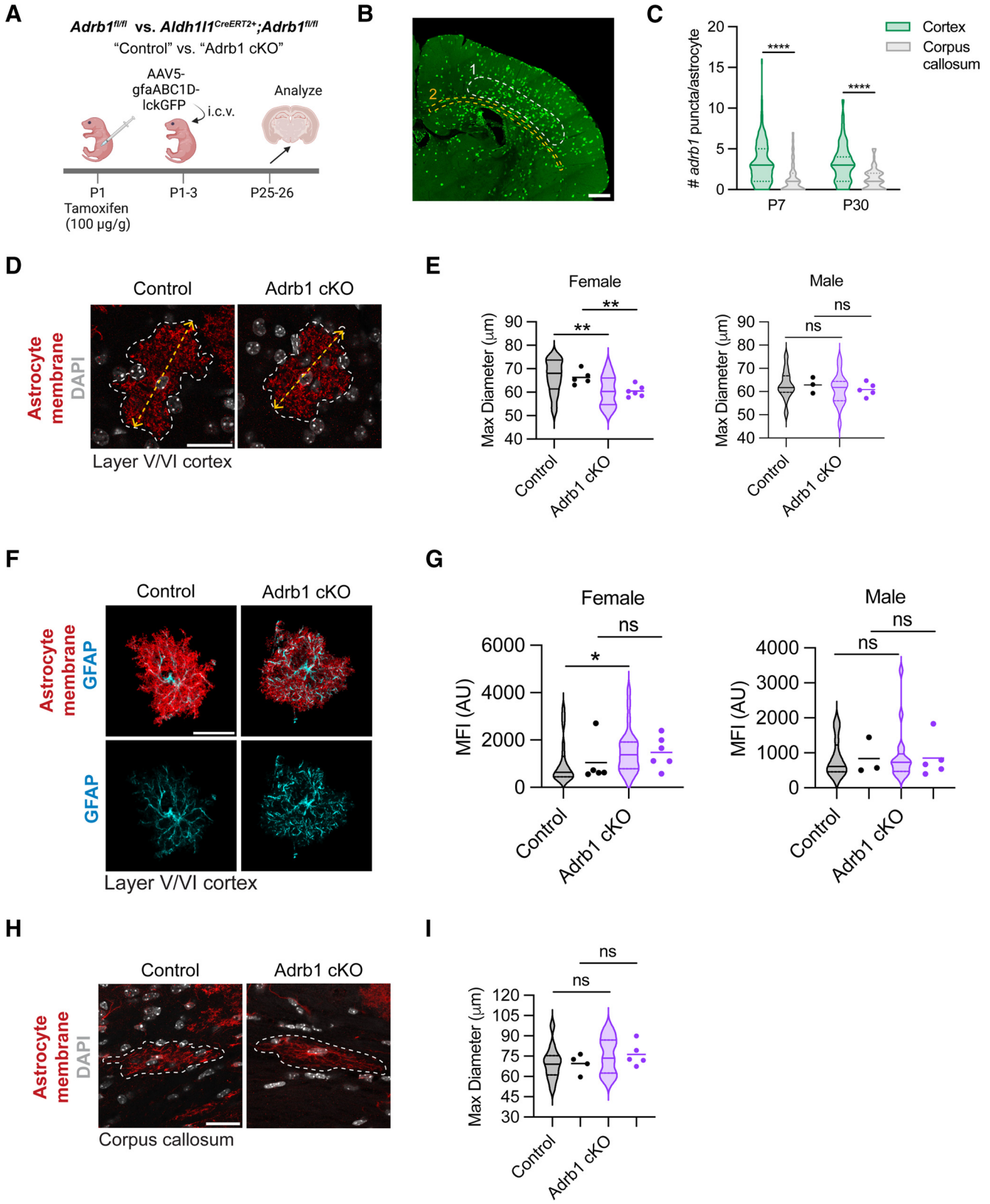

Figure 6. Noradrenergic signaling through the astrocytic β_1-adrenergic receptor increases gray matter astrocyte size in female mice. ***A***, Schematic of astrocyte sparse labeling experimental paradigm in control or Adrb1 cKO littermates. ***B***, Representative image of sparse astrocyte labeling with AAV5-gfaABC1D-lckGFP reporter virus, with ROIs analyzed highlighted with dotted circles. 1, layer V/VI of somatosensory cortex; 2, corpus callosum. Scale bar, 500 μm. ***C***, Quantification of per-astrocyte *Adrb1* expression at P7 versus P30, in gray matter (cortex) versus white matter (corpus callosum). P7 statistics: Mann–Whitney test ($U_{(252)} = 3566$, $^{****}p < 0.0001$). P30 statistics: Mann–Whitney test ($U_{(171)} = 1631$, $^{****}p < 0.0001$). ***D***, Representative images of cortical astrocytes in control or Adrb1 cKO littermates. Yellow dashed arrow indicates maximum diameter. Scale bar, 25 μm. ***E***, Quantification of cortical astrocyte maximum diameter in female and male animals. Median ± interquartile range (violin plots) represent individual cells. Dots represent individual mice (WT F, 5; Adrb1 cKO F, 6; WT M, 3; Adrb1 cKO M, 5). Data from 3-5 cells were averaged per mouse. Female statistics: two-tailed unpaired *t* test, run on per-cell data ($t_{(43)} = 2.877$, $^{**}p = 0.00602$); two-tailed unpaired *t* test, run on per-mouse data ($t_{(9)} =$

adapted their morphology to match the gray versus white matter regions where they reside (X. Han et al., 2013). Neurons can directly impact astrocyte morphology through, for example, the release of the secreted morphogen sonic hedgehog (Farmer et al., 2016). However, immature cortical astrocytes transplanted into the cerebellum of developing (P5-P8) mice still retain many aspects of their original cortical structural and molecular identity, suggesting that some aspects of astrocyte heterogeneity may be cell-intrinsic (Chierzi et al., 2023). Here, we show that noradrenergic projections are enriched in gray relative to white matter and that NE signaling preferentially impacts gray matter astrocyte morphology during brain development. Our data add to evidence that neuronal cues, in this case, differentially enriched between gray and white matter, may contribute to the morphologic distinctions between gray and white matter astrocytes.

We further identify the β_1-adrenergic receptor on astrocytes as a relevant target of NE signaling during brain development, impacting both astrocyte morphology and some aspects of behavior. This is timely, since most studies of NE in astrocytes have focused on the α_1-adrenergic receptor and its role in calcium fluctuations in adult astrocytes (Ding et al., 2013; Ma et al., 2016; Chen et al., 2020). Our *in vitro* data suggested that stimulation of every arm (α_1, α_2, and β) of the adrenergic signaling pathway affected astrocyte branching (Fig. 4*E*, *F*). It is intriguing that stimulation of receptors with opposing effects on cAMP levels (β increases; α_2 decreases; Fig. 4*A*) also had opposing effects on astrocyte branching. Previous work has shown that cAMP or a direct activator of adenylate cyclase both rapidly promote process extension in cultured astrocytes (Shain et al., 1987; Kitano et al., 2021). Moreover, local cAMP levels regulate filopodia formation in surveilling microglia (Bernier et al., 2019). Together, this suggests cAMP or its downstream products may promote astrocytic process formation in both developing and adult organisms.

Our study also contributes to an appreciation of how environmental cues, such as NE, can shape astrocyte morphology. Our *in vitro* studies suggest that this effect may be quite rapid, consistent with a broad literature showing, for example, that astrocytes can respond to parturition or water deprivation with morphologic changes within hours (Theodosis and Poulain, 1993). In the hippocampus, astrocytes frequently extend and retract processes from dendritic spines, with dynamic changes occurring over minutes (Haber et al., 2006). Furthermore, the morphology of astrocytes, particularly in their fine branches, has direct impacts on synaptic function (Pannasch et al., 2014; Badia-Soteras et al., 2023). Our data suggest that noradrenergic signaling during development can affect the structure of astrocytes, thereby potentially influencing their synaptic functions. Future studies would benefit from higher resolution imaging modalities, such as electron microscopy (Pannasch et al., 2014) or superresolution microscopy (Arizono et al., 2020) to better appreciate the structural details of astrocyte fine processes, which can be 10-100 nm in diameter (Khakh and Sofroniew, 2015).

We further found that loss of astrocytic β_1 signaling during development led to adult deficits in balance beam performance and PPI preferentially impacting female animals. This is consistent with our finding that astrocyte-conditional loss of β_1 signaling decreases cortical astrocyte size only in female animals. We did find that astrocytic *Adrb1* expression varied by sex (Fig. 3*F*), suggesting that baseline receptor expression differences could mediate the sex specificity of our morphologic and behavioral findings. Notably, we did not observe sex-specific differences in NE projection density at P30 (Fig. 1*D*). There is precedent for the NE system to have sex-specific effects, including differential gene expression in the locus coeruleus of male versus female mice (Mulvey et al., 2018). Clinical studies show a higher incidence of major depression and post-traumatic stress disorder in women, and suggest that women have, at baseline, a heightened state of NE arousal (Bangasser et al., 2016). Thus, baseline differences in arousal or stress responses in male versus female animals could also contribute to these findings.

Importantly, determining whether these findings are relevant to human conditions requires a better understanding of the similarities between mouse and human noradrenergic systems during development. We found that NE projection density was significantly greater in the gray matter versus the white matter in both mouse and human developing brains (Fig. 1). This is consistent with the idea that the NE system may be particularly relevant in gray matter maturation. It also raises the possibility that similar principles could apply to gray versus white matter astrocyte heterogeneity in both species. However, we noticed many striking distinctions between mouse and human noradrenergic development. First, there was a much lower density of NE projections in the human brain (Fig. 1*E-G*) relative to the mouse. Interestingly, this is also observed in nonhuman primates, where dopaminergic projections are found at a notably higher density than noradrenergic projections (Lewis and Morrison 1989; Rosenberg and Lewis 1995). It is interesting to speculate that arousal is heightened in prey species, like rodents, relative to primates. Second, NE projection density increases steadily in the mouse brain and plateaus before adulthood (~P30, a potential "adolescent" time period) in the mouse. In contrast, the peak of NE density projection is at or around term gestation in humans. In rodents, the rate of astrocyte maturation as assessed by morphology tracks closely with the time course of NE process enrichment (Morel et al., 2014; Stogsdill et al., 2017). Evidence from human organoids matured *in vitro* suggests a similar maturation pattern in humans, as the transition from a fetal to mature astrocyte identity occurs in what would be mid-second trimester (Sloan et al., 2017), although data from *in vivo* human brain suggests that astrocyte molecular maturation continues well into postnatal life (Kang et al., 2011). Further detailed studies of human astrocyte maturation and noradrenergic tone across the lifespan could shed light on the relevance of this pathway to human brain development.

←

3.587, $^{**}p = 0.00509$). Male statistics: two-tailed unpaired *t* test, run on per-cell data ($t_{(27)} = 0.7651$, ns, $p = 0.4509$); two-tailed unpaired *t* test, run on per-mouse data ($t_{(6)} = 0.8558$, ns, $p = 0.4249$). ***F***, Representative images of GFAP expression per cortical astrocyte. Images represent the masked lckGFP (red) and GFAP (cyan) signal from an Imaris surface reconstruction of a single cortical astrocyte. Scale bar, 25 μm. ***G***, Quantification of per-cell GFAP expression in female and male animals. Median ± interquartile range (violin plots) represent individual cells. Dots represent individual mice (WT F, 5; Adrb1 cKO F, 6; WT M, 3; Adrb1 cKO M, 5). AU, Arbitrary units. Data from 3-5 cells were averaged per mouse. Female statistics: Mann–Whitney test, run on per-cell data ($U_{(44)} = 157$, $^{*}p = 0.0221$); Mann–Whitney test, run on per-mouse data ($U_{(9)} = 9$, ns, $p = 0.3290$). Male statistics: Mann–Whitney test, run on per-cell data ($U_{(27)} = 100$, ns, $p = 0.9479$); Mann–Whitney test, run on per-mouse data ($U_{(6)} = 7$, ns, $p > 0.9999$). ***H***, Representative images of corpus callosum astrocytes in control or *Adrb1* cKO littermates. White line indicates border of cell. Scale bar, 25 μm. ***I***, Quantification of corpus callosum astrocyte maximum diameter. Median ± interquartile range (violin plots) represent individual cells. Dots represent individual mice (WT, 4; Adrb1 cKO, 5). Data from 2-4 cells were averaged per mouse. Statistics: two-tailed unpaired *t* test, run on per-cell data ($t_{(26)} = 1.233$, $p = 0.2286$); two-tailed unpaired *t* test, run on per-mouse data ($t_{(7)} = 1.233$, ns, $p = 0.2573$).

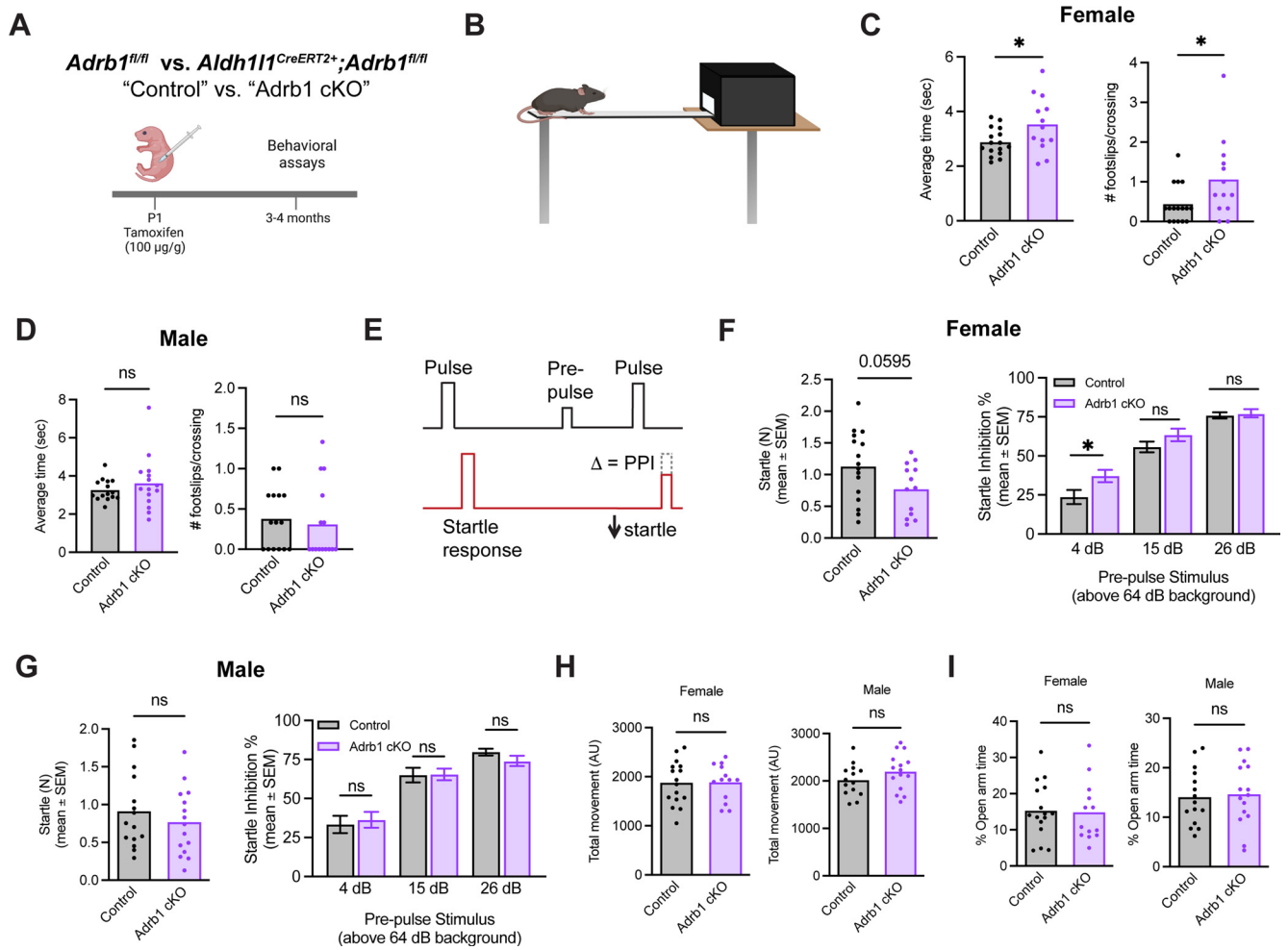

Figure 7. Early postnatal astrocyte-conditional loss of β_1-adrenergic receptor impairs motor coordination and increases PPI in female animals. ***A***, Experimental overview. ***B***, Schematic of balance beam assay. ***C***, Latency to cross balance beam, and accuracy of crossing (foot slips) in female animals, averaged across three trials. Statistics: two-tailed unpaired *t* test (latency to cross, $t_{(27)} = 2.264$, $^*p = 0.0318$; foot slips, $t_{(27)} = 2.201$, $^*p = 0.0365$). Dots represent individual mice. ***D***, Latency to cross balance beam, and accuracy of crossing (foot slips) in male animals, averaged across three trials. Statistics: two-tailed unpaired *t* test (latency to cross, $t_{(28)} = 0.9069$, ns, $p = 0.3722$; foot slips, $t_{(28)} = 0.4337$, ns, $p = 0.6679$). Dots represent individual mice. ***E***, Schematic of PPI assay design. Average interstimulus interval = 15 s (8-22 s). ***F***, Baseline startle and PPI in female animals. Statistics: two-tailed unpaired *t* test (baseline startle, $t_{(27)} = 1.968$, ns, $p = 0.0595$) and two-way ANOVA with Sidak's multiple comparisons (PPI, prepulse × genotype, $F_{(1,27)} = 3.755$, ns, $p = 0.0632$; multiple comparisons, each between genotypes per prepulse stimulus intensity, 4 dB, $^*p = 0.0260$; 15 dB, ns, $p = 0.3418$; 26 dB, ns, $p = 0.9905$). Dots represent individual mice. PPI data are mean ± SEM. ***G***, Baseline startle and PPI in male animals. Statistics: two-tailed unpaired *t* test (baseline startle, $t_{(28)} = 0.8280$, ns, $p = 0.4147$) and two-way ANOVA with Sidak's multiple comparisons (PPI, prepulse × genotype, $F_{(1,28)} = 0.02497$, ns, $p = 0.8756$; multiple comparisons, each between genotype per prepulse stimulus intensity, 4 dB, ns, $p = 0.9452$; 15 dB, ns, $p = 0.9999$; 26 dB, ns, $p = 0.7251$). Dots represent individual mice. PPI data are mean ± SEM. ***H***, Total movement in open field test in female and male animals. Statistics: two-tailed unpaired *t* test (females, $t_{(27)} = 0.06642$, ns, $p = 0.9475$; males, $t_{(27)} = 1.347$, ns, $p = 0.1892$). Dots represent individual mice. ***I***, Percent of time spent in the open arm in elevated plus maze in female and male animals. Statistics: two-tailed unpaired *t* test (females, $t_{(27)} = 0.1553$, ns, $p = 0.8777$; males, $t_{(28)} = 0.2711$, ns, $p = 0.7883$). Dots represent individual mice.

Ultimately, this study raises many interesting possibilities for future studies of astrocyte involvement in brain physiology and pathology. NE is a key neuromodulator, capable of impacting many brain states, including arousal, sleep, learning, and response to stress (Sara, 2009). Thus, identifying a role for noradrenergic signaling in astrocyte development and adult behavior highlights the possibility that homeostatic and disease states which alter noradrenergic tone may also alter brain function via astrocytes. Indeed, a recent study found that activation of the locus coeruleus, via chemogenetics or optogenetics, upregulates a set of genes that are strongly enriched in astrocytes (Privitera et al., 2023). Astrocytes are exquisitely sensitive to local environmental, immune, and systemic cues, and they retain this sensitivity well into adulthood. A better understanding of the regulatory factors that influence an astrocyte's state could thus improve our ability to manipulate astrocytes for therapeutic purposes.

References

Allen NJ, Bennett ML, Foo LC, Wang GX, Chakraborty C, Smith SJ, Barres BA (2012) Astrocyte glypicans 4 and 6 promote formation of excitatory synapses via GluA1 AMPA receptors. Nature 486:410–414.

Anders S, Pyl PT, Huber W (2015) HTSeq: a Python framework to work with high-throughput sequencing data. Bioinformatics 31:166–169.

Anderson CM, Swanson RA (2000) Astrocyte glutamate transport: review of properties, regulation, and physiological functions. Glia 32:1–14.

Arizono M, et al. (2020) Structural basis of astrocytic Ca^{2+} signals at tripartite synapses. Nat Commun 11:1906.

Arshadi C, Günther U, Eddison M, Harrington KI, Ferreira TA (2021) SNT: a unifying toolbox for quantification of neuronal anatomy. Nat Methods 18:374–377.

Badia-Soteras A, et al. (2023) Retraction of astrocyte leaflets from the synapse enhances fear memory. Biol Psychiatry 94:226–238.

Bangasser DA, Wiersielis KR, Khantsis S (2016) Sex differences in the locus coeruleus-norepinephrine system and its regulation by stress. Brain Res 1641:177–188.

Batiuk MY, De Vin F, Duqué SI, Li C, Saito T, Saido T, Fiers M, Grant Belgard T, Holt MG (2017) An immunoaffinity-based method for isolating ultrapure adult astrocytes based on ATP1B2 targeting by the ACSA-2 antibody. J Biol Chem 292:8874–8891.

Batiuk MY, et al. (2020) Identification of region-specific astrocyte subtypes at single cell resolution. Nat Commun 11:1–15.

Bayraktar OA, Fuentealba LC, Alvarez-Buylla A, Rowitch DH (2014) Astrocyte development and heterogeneity. Cold Spring Harb Perspect Biol 7:a020362.

Bayraktar OA, et al. (2020) Astrocyte layers in the mammalian cerebral cortex revealed by a single-cell in situ transcriptomic map. Nat Neurosci 23:500–509.

Bellot-Saez A, Kékesi O, Morley JW, Buskila Y (2017) Astrocytic modulation of neuronal excitability through K^+ spatial buffering. Neurosci Biobehav Rev 77:87–97.

Bernier LP, et al. (2019) Nanoscale surveillance of the brain by microglia via cAMP-regulated filopodia. Cell Rep 27:2895–2908.e4.

Bushong EA, Martone ME, Jones YZ, Ellisman MH (2002) Protoplasmic astrocytes in CA1 stratum radiatum occupy separate anatomical domains. J Neurosci 22:183–192.

Chen J, Poskanzer KE, Freeman MR, Monk KR (2020) Live-imaging of astrocyte morphogenesis and function in zebrafish neural circuits. Nat Neurosci 23:1297–1306.

Chierzi S, Kacerovsky JB, Fok AH, Lahaie S, Shibi-Rosen A, Farmer WT, Murai KK (2023) Astrocytes transplanted during early postnatal development integrate, mature, and survive long-term in mouse cortex. J Neurosci 43:1509–1529.

Christopherson KS, Ullian EM, Stokes CC, Mullowney CE, Hell JW, Agah A, Lawler J, Mosher DF, Bornstein P, Barres BA (2005) Thrombospondins are astrocyte-secreted proteins that promote CNS synaptogenesis. Cell 120:421–433.

Chung WS, et al. (2013) Astrocytes mediate synapse elimination through MEGF10 and MERTK pathways. Nature 504:394–400.

Clavreul S, et al. (2019) Cortical astrocytes develop in a plastic manner at both clonal and cellular levels. Nat Commun 10:4884.

Ding F, O'Donnell J, Thrane AS, Zeppenfeld D, Kang H, Xie L, Wang F, Nedergaard M (2013) α1-Adrenergic receptors mediate coordinated Ca^{2+} signaling of cortical astrocytes in awake, behaving mice. Cell Calcium 14:384–399.

Dobin A, Davis CA, Schlesinger F, Drenkow J, Zaleski C, Jha S, Batut P, Chaisson M, Gingeras TR (2013) STAR: ultrafast universal RNA-Seq aligner. Bioinformatics 29:15–21.

Elias M, Deacon T, Caviness VS (1982) The development of neocortical noradrenergic innervation in the mouse: a quantitative radioenzymatic analysis. Dev Brain Res 255:652–656.

Farmer WT, et al. (2016) Neurons diversify astrocytes in the adult brain through sonic hedgehog signaling. Science 351:849–854.

Finnema SJ, et al. (2016) Imaging synaptic density in the living human brain. Sci Transl Med 8:348ra96.

Foo LC (2013) Purification of rat and mouse astrocytes by immunopanning. Cold Spring Harb Protoc 2013:421–432.

Foo LC, et al. (2011) Development of a method for the purification and culture of rodent astrocytes. Neuron 71:799–811.

Fu Q, Xiang YK (2015) Trafficking of β-adrenergic receptors. In: Progress in molecular biology and translational science, pp 151–188. Amsterdam: Elsevier.

Haber M, Zhou L, Murai KK (2006) Cooperative astrocyte and dendritic spine dynamics at hippocampal excitatory synapses. J Neurosci 26:8881–8891.

Han RT, Vainchtein ID, Schlachetzki JC, Cho FS, Dorman LC, Ahn E, Kim DK, Barron JJ, Nakao-Inoue H, Molofsky AB, Glass CK, Paz JT, Molofsky AV (2023) Microglial pattern recognition via IL-33 promotes synaptic refinement in developing corticothalamic circuits in mice. J Exp Med 220:e20220605.

Han X, Chen M, Wang F, Windrem M, Wang S, Shanz S, Xu Q, Oberheim NA, Bekar L, Betstadt S, Silva AJ, Takano T, Goldman SA, Nedergaard M (2013) Forebrain engraftment by human glial progenitor cells enhances synaptic plasticity and learning in adult mice. Cell Stem Cell 12:342–353.

Herrero-Navarro Á, Puche-Aroca L, Moreno-Juan V, Sempere-Ferràndez A, Espinosa A, Susín R, Torres-Masjoan L, Leyva-Díaz E, Karow M, Figueres-Oñate M, López-Mascaraque L, López-Atalaya JP, Berninger B, López-Bendito G (2021) Astrocytes and neurons share region-specific transcriptional signatures that confer regional identity to neuronal reprogramming. Sci Adv 7:eabe8978.

Jaim-Etcheverry G, Zieher LM (1980) DSP-4: a novel compound with neurotoxic effects on noradrenergic neurons of adult and developing rats. Brain Res 188:513–523.

Kang HJ, et al. (2011) Spatio-temporal transcriptome of the human brain. Nature 478:483–489.

Khakh BS, Sofroniew MV (2015) Diversity of astrocyte functions and phenotypes in neural circuits. Nat Neurosci 18:942–952.

Kitano T, Eguchi R, Okamatsu-Ogura Y, Yamaguchi S, Otsuguro K-i (2021) Opposing functions of α- and β-adrenoceptors in the formation of processes by cultured astrocytes. J Pharmacol Sci 145:228–240.

Krawczyk MC, et al. (2022) Human astrocytes exhibit tumor microenvironment-, age-, and sex-related transcriptomic signatures. J Neurosci 42:1587–1603.

Lanjakornsiripan D, Pior BJ, Kawaguchi D, Furutachi S, Tahara T, Katsuyama Y, Suzuki Y, Fukazawa Y, Gotoh Y (2018) Layer-specific morphological and molecular differences in neocortical astrocytes and their dependence on neuronal layers. Nat Commun 9:1623.

Latsari M, Dori I, Antonopoulos J, Chiotelli M, Dinopoulos A (2002) Noradrenergic innervation of the developing and mature visual and motor cortex of the rat brain: a light and electron microscopic immunocytochemical analysis. J Comp Neurol 445:145–58.

Lewis DA, Morrison JH (1989) Noradrenergic innervation of monkey prefrontal cortex: a dopamine-β-hydroxylase immunohistochemical study. J Comp Neurol 282:317–330.

Love MI, Huber W, Anders S (2014) Moderated estimation of fold change and dispersion for RNA-Seq data with DESeq2. Genome Biol 15:550.

Lundgaard I, Osório MJ, Kress BT, Sanggaard S, Nedergaard M (2014) White matter astrocytes in health and disease. Neuroscience 276:161–73.

Ma Z, Stork T, Bergles DE, Freeman MR (2016) Neuromodulators signal through astrocytes to alter neural circuit activity and behaviour. Nature 539:428–432.

Mani BK, Osborne-Lawrence S, Vijayaraghavan P, Hepler C, Zigman JM (2016) β1-Adrenergic receptor deficiency in Ghrelin-expressing cells causes hypoglycemia in susceptible individuals. J Clin Invest 126:3467–3478.

Molofsky AV, Krenick R, Ullian E, Tsai HH, Deneen B, Richardson WD, Barres BA, Rowitch DH (2012) Astrocytes and disease: a neurodevelopmental perspective. Genes Dev 26:891–907.

Molofsky AV, Kelley KW, Tsai HH, Redmond SA, Chang SM, Madireddy L, Chan JR, Baranzini SE, Ullian EM, Rowitch DH (2014) Astrocyte-encoded positional cues maintain sensorimotor circuit integrity. Nature 509:189–194.

Morel L, Higashimori H, Tolman M, Yang Y (2014) $VGluT1^+$ neuronal glutamatergic signaling regulates postnatal developmental maturation of cortical protoplasmic astroglia. J Neurosci 34:10950–10962.

Mulvey B, Bhatti DL, Gyawali S, Lake AM, Kriaucionis S, Ford CP, Bruchas MR, Heintz N, Dougherty JD (2018) Molecular and functional sex differences of noradrenergic neurons in the mouse locus coeruleus. Cell Rep 23:2225–2235.

Nowak P (2016) Selective lifelong destruction of brain monoaminergic nerves through perinatal DSP-4 treatment. Curr Top Behav Neurosci 29:51–71.

O'Donnell J, Zeppenfeld D, McConnell E, Pena S, Nedergaard M (2012) Norepinephrine: a neuromodulator that boosts the function of multiple cell types to optimize CNS performance. Neurochem Res 37:2496–2512.

Oke A, Solnick J, Adams RN (1983) Catecholamine distribution patterns in rat thalamus. Brain Res 269:180–183.

Pannasch U, Freche D, Dallérac G, Ghézali G, Escartin C, Ezan P, Cohen-Salmon M, Benchenane K, Abudara V, Dufour A, Lübke JH, Déglon N, Knott G, Holcman D, Rouach N (2014) Connexin 30 sets synaptic strength by controlling astroglial synapse invasion. Nat Neurosci 17:549–558.

Paukert M, Agarwal A, Cha J, Doze VA, Kang JU, Bergles DE (2014) Norepinephrine controls astroglial responsiveness to local circuit activity. Neuron 82:1263–1270.

Philipp M, Hein L (2004) Adrenergic receptor knockout mice: distinct functions of 9 receptor subtypes. Pharmacol Ther 101:65–74.

Poskanzer KE, Molofsky AV (2018) Dynamism of an astrocyte in vivo: perspectives on identity and function. Annu Rev Physiol 80:143–157.

Privitera M, von Ziegler A, Floriou-Servou SN, Duss Runzhong Zhang S, Leimbacher O, Sturman R, Waag FK, Roessler A, Heylen Y, Vermeiren D, Van Dam PP, Deyn D, Bohacek J (2023) Noradrenaline release from the locus coeruleus shapes stress-induced hippocampal gene expression. eLife 12:RP88559.

Rosenberg DR, Lewis DA (1995) Postnatal maturation of the dopaminergic innervation of monkey prefrontal and motor cortices: a tyrosine hydroxylase immunohistochemical analysis. J Comp Neurol 358:383–400.

Sara SJ (2009) The locus coeruleus and noradrenergic modulation of cognition. Nat Rev Neurosci 10:211–223.

Semple BD, Blomgren K, Gimlin K, Ferriero DM, Noble-Haeusslein LJ (2013) Brain development in rodents and humans: identifying benchmarks of maturation and vulnerability to injury across species. Prog Neurobiol 106:1–16.

Shain W, Forman DS, Madelian V, Turner JN (1987) Morphology of astroglial cells is controlled by beta-adrenergic receptors. J Cell Biol 105:2307–2314.

Sherpa AD, Xiao F, Joseph N, Aoki C, Hrabetova S (2016) Activation of β-adrenergic receptors in rat visual cortex expands astrocytic processes and reduces extracellular space volume. Synapse 70:307–316.

Sloan SA, Darmanis S, Huber N, Khan TA, Birey F, Caneda C, Reimer R, Quake SR, Barres BA, Paşca SP (2017) Human astrocyte maturation captured in 3D cerebral cortical spheroids derived from pluripotent stem cells. Neuron 95:779–790.e6.

Srinivasan R, Lu TY, Chai H, Xu J, Huang BS, Golshani P, Coppola G, Khakh BS (2016) New transgenic mouse lines for selectively targeting astrocytes and studying calcium signals in astrocyte processes in situ and in vivo. Neuron 92:1181–1195.

Stogsdill JA, Ramirez J, Liu D, Kim YH, Baldwin KT, Enustun E, Ejikeme T, Ru RJ, Eroglu C (2017) Astrocytic neuroligins control astrocyte morphogenesis and synaptogenesis. Nature 551:192–197.

Theodosis DT, Poulain DA (1993) Activity-dependent neuronal-glial and synaptic plasticity in the adult mammalian hypothalamus. Neuroscience 57:501–535.

Vainchtein ID, Chin G, Cho FS, Kelley KW, Miller JG, Chien EC, Liddelow SA, Nguyen PT, Nakao-Inoue H, Dorman LC, Akil O, Joshita S, Barres BA, Paz JT, Molofsky AB, Molofsky AV (2018) Astrocyte-derived interleukin-33 promotes microglial synapse engulfment and neural circuit development. Science 359:1269–1273.